Progress In Electromagnetics Research B, Vol. 82, 93–114, 2018

Full Polarizability Matrix Extraction Formulas for Electrically Small Particles via Reflection/Transmission Coefficients

Theodosios D. Karamanos and Nikolaos V. Kantartzis*

Abstract—A class of rigorous formulas for the efficient extraction of the full polarizability matrix of electrically small particles is introduced in this paper. After the dipole approximation of the scatterer, under study, the latter is placed on a two-dimensional square array, illuminated by four normally incident plane waves, and eventually its polarizabilities are expressed in terms of induced dipole moments. Then, by applying an equivalent surface model for the array, the induced dipoles are calculated as a function of the reflection/transmission coefficients from the array. Lastly, the combination of the previous formulations leads to the final expressions for the polarizability matrix of the particle. In order to verify the featured methodology, the extracted polarizabilities are involved in radar cross section and total radiated power calculations for various incidences and are compared with their simulated counterparts.

1. INTRODUCTION

First-principles homogenization methods have lately gained increased attention due to their theoretical consistency and accuracy. In essence, their primary aim is to analytically calculate the constitutive parameters of an effective bulk medium [1–4] or effective surface [5–10] through the properties of their comprising particles. As a result, weak spatial dispersion is taken into consideration, because the electromagnetic interactions among individual scatterers on the two-dimensional/three-dimensional (2D/3D) grid are incorporated in the analysis. Note that such an approach originates from the Claussius-Mossotti and Maxwell-Garnett formulas, initially applied in the quasi-static spectrum for effective media consisting of dielectric spheres [11]. Basically, the majority of first-principles techniques relies on the dipole approximation of the electromagnetic response of a particle. Thus, the parameters that propotionally link the induced dipole moments with the external field around the particle, namely the polarizabilities, are deemed critical for the related homogenization process, and, subsequently, several approaches have been, hitherto, reported for their precise retrieval. A characteristic representative of these formulations intends to analytically calculate the polarizabilities of a scatterer by presuming an approximate current distribution on it, usually originating from circuit or antenna theory [12, 13]. These schemes, however, are structure-oriented, applicable only to certain particle geometries, and usually produce quasi-static results, valid only for low frequencies. On the other hand, numerical extraction methods have, also, been launched [14, 15], yet bearing the complexity of a computational approach.

Recently, a family of alternative algorithms proposes the extraction of dynamic polarizabilities via the electromagnetic response of the scatterer, modeled in terms of dipole moments. Among them, [16, 17] obtain the desired polarizabilities employing the scattered field from an arbitrary scatterer via experiments or simulations. Nonetheless, the far-field is usually rather cumbersome (if not prohibitive) to experimentally acquire from such small-sized individual particles. To waive this hindrance, the use of the S-parameters or the reflection/transmission coefficients from illuminated 2D

Received 17 July 2018, Accepted 28 September 2018, Scheduled 9 October 2018

* Corresponding author: Nikolaos V. Kantartzis (kant@ece.auth.gr).

The authors are with the Applied and Computational Electromagnetics Laboratory, Department of Electrical and Computer Engineering, Aristotle University of Thessaloniki, GR-54124 Thessaloniki, Greece.

particle arrays can be proven an efficient means for accurate polarizability extraction, hence triggering the development of diverse methods. Firstly, an instructive technique for retrieving the polarizabilities of anisotropic scatterers in terms of closed-form expressions has been developed in [18]. Expanding this concept, the extraction of the polarizability matrix of omega-type bianisotropic structures through the reflection/transmission coefficients of two or, for simplicity, a single 2D particle array has been, respectively, proposed in [19]. Both approaches, however, involve the numerical solution of a non-linear system of equations, which is not always easy to implement. This issue has been successfully addressed in [20], where the ten unknown polarizabilities of a non-planar helix chiral particle are retrieved. Furthermore, an experimental polarizability extraction algorithm has lately appeared, yet its use is confined to anisotropic scatterers, like metallic discs or toruses [21], while [22] presents a similar scheme for anisotropic complementary metamaterial scatterers, using the response of rectangular waveguides. Finally, [23] retrieves the full polarizability matrix of an arbitrary small particle by illuminating both sides of an infinite 2D array with normally incident plane waves. The basic idea relies on a pre-processing step which obtains the radiation/coupling coefficients of the 2D array via analytically derived quasi-static polarizabilities of metallic spheres. Therefore, its performance depends mainly on the accuracy of the polarizabilities at the frequencies, under study, as well as on the demand for high scattering values from the selected testing inclusions.

In this paper, the full polarizability matrix of electrically small scatterers is systematically retrieved through the reflection/transmission coefficients, using direct and consistently developed matrix-form formulas. Every scatterer is initially assumed to be sufficiently small with respect to the impending wavelength, so that its scattering field can be safely described via a set of electric and magnetic dipole moments. Next, the aforesaid particle is placed on an infinite 2D lattice in vacuum, which is, in turn, illuminated by normally incident plane waves. The subsequent induced dipole moments are calculated as a function of the polarizability matrix and the local field acting at its center. To this end, the interactions amid the particles on the array are rigorously and dynamically computed in terms of fast-converging Green function series, without the involvement of any pre-processing extraction scheme, unlike existing realizations. In parallel, the reflection/transmission coefficients from the different impending waves on the array are evaluated from the induced dipoles through an equivalent surface current model. Hence, by combining these two approaches, a single expression is derived that directly produces the desired polarizabilities on the array plane from the simulated or measured reflection/transmission coefficient matrix. Also, a simplified, yet very instructive, version of the proposed formula is provided for anisotropic and omega-type bianisotropic scatterers, which constitute the majority of contemporary metamaterial applications. Then, the featured algorithm is applied to two characteristic metamaterial scatterers that lack analytical or circuit-model solutions for their polarizabilities, while all results are extensively certified via detailed comparisons of the calculated radar cross sections and total radiated power with the corresponding simulated outcomes, each one obtained for a different angle of incidence. The specific validation process, implemented for the first time to the best of the authors' knowledge, substantiates the robustness and accuracy of the developed methodology at the frequency areas of interest and, concurrently, reveals the wavelegth limits of the dipole approximation for small scatterers.

2. THEORETICAL FORMULATION AND IMPLEMENTATION PRINCIPLES

2.1. Dipole Approximation of a Small Scatterer 2D Array

Let us consider a Cartesian coordinate system set at the center of an arbitrary scatterer, such as the sphere displayed in the inlet of Fig. 1. We, also, presume that the specific particle is sufficiently smaller than the wavelength of the incident field (initial assumption: $2s \leq \lambda_{\text{inc}}/4$, with $2s$ the largest dimension of the scatterer), so that its scattered field may be described only in terms of electric and magnetic dipoles. Then, the scatterer can be represented with an electric dipole moment, $\mathbf{p}$, and a magnetic dipole moment, $\mathbf{m}$, whose relation to the local electric and magnetic fields at the center of the particle, $\mathbf{E}^{\text{loc}}$ and $\mathbf{H}^{\text{loc}}$, respectively, is given by

$$\begin{bmatrix} \mathbf{p} \\ c^{-1}\mathbf{m} \end{bmatrix} = \begin{bmatrix} \bar{\bar{\alpha}}_{ee} & \bar{\bar{\alpha}}_{em} \\ \bar{\bar{\alpha}}_{me} & \bar{\bar{\alpha}}_{mm} \end{bmatrix} \cdot \begin{bmatrix} \varepsilon \mathbf{E}^{\text{loc}} \\ c^{-1}\mathbf{H}^{\text{loc}} \end{bmatrix}, \tag{1}$$

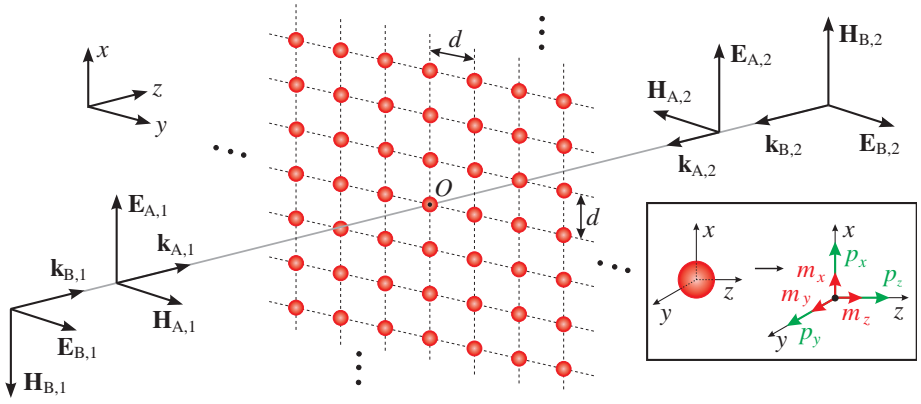

Figure 1. A 2D periodic lattice comprising an infinite number of identical, arbitrary, and electrically small scatterers. Plane waves are normally incident on both sides of the array with perpenticular polarizations to each other, i.e., A and B. Index "1" corresponds to propagation towards the $+z$ direction, while index "2" to propagation towards the $-z$ direction (inlet sketch: An arbitary scatterer with its coorodinate system refering to (1) and (2a) along with its equivalent model constructed via electric and magnetic dipoles placed at its shape center).

or, in vector notation, by $\boldsymbol{\mu} = [\alpha]\,\mathbf{f}^{\text{loc}}$, where $c = 1/\sqrt{\mu\varepsilon}$ is the velocity of light in the surrounding medium. Furthermore, in (1), $\bar{\bar{\alpha}}_{ee}$, $\bar{\bar{\alpha}}_{em}$, $\bar{\bar{\alpha}}_{me}$, and $\bar{\bar{\alpha}}_{mm}$ are the dyads of electric-electric, electric-magnetic, magnetic-electric, and magnetic-magnetic polarizabilities of the particles, while

$$\boldsymbol{\mu} = \left[p_x \;\; p_y \;\; p_z \;\; c^{-1}m_x \;\; c^{-1}m_y \;\; c^{-1}m_z\right]^T, \tag{2a}$$

$$\mathbf{f}^{\text{loc}} = \left[\varepsilon E_x^{\text{loc}} \;\; \varepsilon E_y^{\text{loc}} \;\; \varepsilon E_z^{\text{loc}} \;\; c^{-1}H_x^{\text{loc}} \;\; c^{-1}H_y^{\text{loc}} \;\; c^{-1}H_z^{\text{loc}}\right]^T, \tag{2b}$$

are the vectors of the dipole moments and local fields, respectively.

Employing the prior small scatterer to create an infinite 2D array at the xy-plane, with the orientation of Fig. 1, and illuminating the resulting structure with an arbitrary incident wave, $\mathbf{f}^{\text{loc}}$ can be expressed as

$$\mathbf{f}^{\text{loc}} = \mathbf{f}^{\text{inc}} + \mathbf{f}^{\text{scat}}, \tag{3}$$

with $\mathbf{f}^{\text{inc}}$ the incident and $\mathbf{f}^{\text{scat}}$ the scattered field vector induced at the center of any particle due to the other particles of the array. Moreover, if we assume normally incident plane waves onto the array, as in Fig. 1, all of its dipoles are of the same value, according to Bloch-Floquet analysis [7, 18]. Hence, the scattered field at $O(0,0,0)$, is given by

$$\begin{bmatrix} \varepsilon\mathbf{E}^{\text{scat}} \\ c^{-1}\mathbf{H}^{\text{scat}} \end{bmatrix} = \begin{bmatrix} \bar{\bar{C}}_{ee} & \bar{\bar{C}}_{em} \\ \bar{\bar{C}}_{me} & \bar{\bar{C}}_{mm} \end{bmatrix} \cdot \begin{bmatrix} \mathbf{p}_0 \\ c^{-1}\mathbf{m}_0 \end{bmatrix}, \tag{4}$$

or, in vector notation, by $\mathbf{f}^{\text{scat}} = [C]\,\boldsymbol{\mu}$. The elements of matrix $[C]$, i.e., the interaction coefficients, is infinite series of the proper dyadic Green functions [24], whose values can be analytically obtained through fast converging calculation schemes [25, 26]. Substituting Eqs. (2a) and (3) into Eq. (1), imposing a plane wave illumination along the $\pm z$ directions, and setting vacuum as our background medium, one obtains

$$\boldsymbol{\mu} = [\alpha]\left\{\mathbf{f}^{\text{inc}} + [C]\boldsymbol{\mu}\right\} \Rightarrow \tag{5}$$

$$\begin{bmatrix} p_x \\ p_y \\ c_0^{-1}m_x \\ c_0^{-1}m_y \end{bmatrix} = \begin{bmatrix} \alpha_{ee}^{xx} & \alpha_{ee}^{xy} & \alpha_{em}^{xx} & \alpha_{em}^{xy} \\ \alpha_{ee}^{yx} & \alpha_{ee}^{yy} & \alpha_{em}^{yx} & \alpha_{em}^{yy} \\ \alpha_{me}^{xx} & \alpha_{me}^{xy} & \alpha_{mm}^{xx} & \alpha_{mm}^{xy} \\ \alpha_{me}^{yx} & \alpha_{me}^{yy} & \alpha_{mm}^{yx} & \alpha_{mm}^{yy} \end{bmatrix} \cdot \left\{ \begin{bmatrix} \varepsilon_0 E_x^{\text{inc}} \\ \varepsilon_0 E_y^{\text{inc}} \\ c_0^{-1}H_x^{\text{inc}} \\ c_0^{-1}H_y^{\text{inc}} \end{bmatrix} + \begin{bmatrix} C_{ee}^{xx} & C_{ee}^{xy} & C_{em}^{xx} & C_{em}^{xy} \\ C_{ee}^{yx} & C_{ee}^{yy} & C_{em}^{yx} & C_{em}^{yy} \\ C_{me}^{xx} & C_{me}^{xy} & C_{mm}^{xx} & C_{mm}^{xy} \\ C_{me}^{yx} & C_{me}^{yy} & C_{mm}^{yx} & C_{mm}^{yy} \end{bmatrix} \cdot \begin{bmatrix} p_x \\ p_y \\ c_0^{-1}m_x \\ c_0^{-1}m_y \end{bmatrix} \right\}, \tag{6}$$

where dipole moments p_z and m_z have been omitted, since they are normal to the plane of the array and, thus, they do not contribute to the scattering interactions [7,18]. Based on the properties of dyadic Green functions [18, 24], for a normally incident plane wave, it holds that $C_{em}^{ij} = C_{me}^{ji} = 0$, where $i, j = x, y$. In addition, C_{ee}^{ij} and C_{mm}^{ij}, for $i \neq j$, are much smaller than C_{ee}^{ii} and C_{mm}^{ii}, and can be safely set to zero ($C_0^{xy} \approx 0$, see Appendix A); a convention which renders $[C]$ a diagonal matrix. Finally, for a square 2D array, as the proposed setup of Fig. 1, it occurs that $C_{ee}^{ii} = C_{mm}^{ii} = C_0^{xx} = C_0$, hence $[C] = C_0\, I$, with I the identity matrix. Note that, in this paper, C_0 is analytically evaluated by means of dyadic Green functions (see Appendix B), although it may be alternatively extracted from the S-parameters or the reflection/transmission coefficients, for a reduced accuracy [20, 23].

In this context, Eq. (6) reveals that, if the unknowns are the polarizabilities of the scatterer on the xy-plane, they can be retrieved via the inversion of a linear system of 16 independent equations. Since the induced dipole moments of a scatterer, for a given set of polarizabilities, are a function of the incident field on its surface, the required equations may be acquired from four distinct incident waves on the array, as illustrated in Fig. 1. Specifically, the two polarizations perpendicular to each other, and propagating towards the $\pm z$ directions, will be utilized, or, for $|\mathbf{E}| = 1\,\mathrm{V/m}$,

$$\mathbf{f}_{xOy}^{\mathrm{inc}} = \begin{bmatrix} \varepsilon_0 E_x^{\mathrm{inc}} & \varepsilon_0 E_y^{\mathrm{inc}} & c_0^{-1} H_x^{\mathrm{inc}} & c_0^{-1} H_y^{\mathrm{inc}} \end{bmatrix}^T, \quad (7a)$$

$$\mathbf{f}_{\mathrm{A},1}^{\mathrm{inc}} = \varepsilon_0 \begin{bmatrix} 1 & 0 & 0 & 1 \end{bmatrix}^T, \quad \mathbf{f}_{\mathrm{A},2}^{\mathrm{inc}} = \varepsilon_0 \begin{bmatrix} 1 & 0 & 0 & -1 \end{bmatrix}^T, \quad \mathbf{f}_{\mathrm{B},1}^{\mathrm{inc}} = \varepsilon_0 \begin{bmatrix} 0 & 1 & -1 & 0 \end{bmatrix}^T, \quad \mathbf{f}_{\mathrm{B},2}^{\mathrm{inc}} = \varepsilon_0 \begin{bmatrix} 0 & 1 & 1 & 0 \end{bmatrix}^T. \quad (7b)$$

By plugging all Eq. (7a) into Eq. (6), the desired polarizabilities of our scatterer on the xy-plane can be expressed as a function of the induced dipole moments in the form of

$$[M_{\mathrm{t}}] = [\alpha]\big\{[F_1] + C_0[M_{\mathrm{t}}]\big\} \Rightarrow [\alpha]^{-1} = [F_1][M_{\mathrm{t}}]^{-1} + C_0\, I, \quad (8)$$

where

$$[M_{\mathrm{t}}] = \begin{bmatrix} \boldsymbol{\mu}_1^{\mathrm{A}} & \boldsymbol{\mu}_2^{\mathrm{A}} & \boldsymbol{\mu}_1^{\mathrm{B}} & \boldsymbol{\mu}_2^{\mathrm{B}} \end{bmatrix} = \begin{bmatrix} p_{x,1}^{\mathrm{A}} & p_{x,2}^{\mathrm{A}} & p_{x,1}^{\mathrm{B}} & p_{x,2}^{\mathrm{B}} \\ p_{y,1}^{\mathrm{A}} & p_{y,2}^{\mathrm{A}} & p_{y,1}^{\mathrm{B}} & p_{y,2}^{\mathrm{B}} \\ c_0^{-1} m_{x,1}^{\mathrm{A}} & c_0^{-1} m_{x,2}^{\mathrm{A}} & c_0^{-1} m_{x,1}^{\mathrm{B}} & c_0^{-1} m_{x,2}^{\mathrm{B}} \\ c_0^{-1} m_{y,1}^{\mathrm{A}} & c_0^{-1} m_{y,2}^{\mathrm{A}} & c_0^{-1} m_{y,1}^{\mathrm{B}} & c_0^{-1} m_{y,2}^{\mathrm{B}} \end{bmatrix}, \quad (9a)$$

$$[F_1] = \begin{bmatrix} \mathbf{f}_{\mathrm{A},1}^{\mathrm{inc}} & \mathbf{f}_{\mathrm{A},2}^{\mathrm{inc}} & \mathbf{f}_{\mathrm{B},1}^{\mathrm{inc}} & \mathbf{f}_{\mathrm{B},2}^{\mathrm{inc}} \end{bmatrix} = \varepsilon_0 \begin{bmatrix} 1 & 1 & 0 & 0 \\ 0 & 0 & 1 & 1 \\ 0 & 0 & -1 & 1 \\ 1 & -1 & 0 & 0 \end{bmatrix}, \quad (9b)$$

with $\boldsymbol{\mu}_1^{\mathrm{A}}, \boldsymbol{\mu}_2^{\mathrm{A}}, \boldsymbol{\mu}_1^{\mathrm{B}}, \boldsymbol{\mu}_2^{\mathrm{B}}$ the induced dipoles from the respective incident fields on the array, $\mathbf{f}_{\mathrm{A},1}^{\mathrm{inc}}, \mathbf{f}_{\mathrm{A},2}^{\mathrm{inc}}, \mathbf{f}_{\mathrm{B},1}^{\mathrm{inc}}, \mathbf{f}_{\mathrm{B},2}^{\mathrm{inc}}$, as described in Fig. 1. It should be stressed that Eq. (8) dictates that the knowledge of the $[M_{\mathrm{t}}]$ dipoles leads directly to the elements of $[\alpha]$. Therefore, the problem of extracting the polarizabilities of a small scatterer reduces to the calculation of the required dipole moments from the response of the 2D array for the respective excitations.

2.2. Induced Dipole Moments Evaluation via Scattered Fields

To compute the required dipole moments, the array of Fig. 1 is replaced by a set of equivalent radiating surfaces. Following the averaging process described in [7, 19, 20], the currents of these surfaces can be expressed in terms of the induced dipole moments as

$$\mathbf{J}_s = \mathbf{J}_{sx} + \mathbf{J}_{sy} = \frac{j\omega p_x}{d^2}\,\hat{\mathbf{x}} + \frac{j\omega p_y}{d^2}\hat{\mathbf{y}}, \qquad \mathbf{K}_s = \mathbf{K}_{sx} + \mathbf{K}_{sy} = \frac{j\omega\mu_0 m_x}{d^2}\,\hat{\mathbf{x}} + \frac{j\omega\mu_0 m_y}{d^2}\,\hat{\mathbf{y}}. \quad (10)$$

Furthermore, as presented in Fig. 2, by applying the appropriate boundary conditions for the surface currents of Eq. (10), the propagating scattered fields from each equivalent surface can be calculated via

$$\mathbf{E}^{\mathrm{surf}} = E_x^{\mathrm{surf}}\hat{\mathbf{x}} + E_y^{\mathrm{surf}}\hat{\mathbf{y}}, \quad (11a)$$

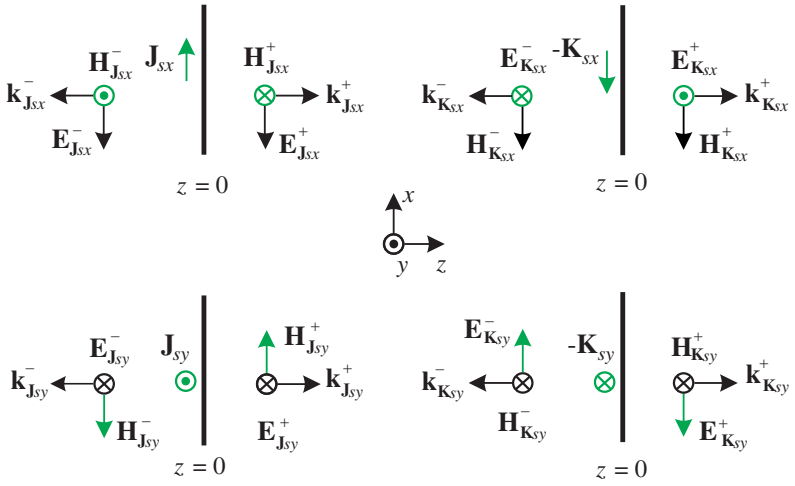

Figure 2. The equivalent surface electric and magnetic current densities of (10) and the corresponding scattered fields of (11), after the application of Ampère's law. The origin of the coordinate system is set at $(x, y, z) = (0, 0, 0)$, while the "+" or "−" sign designates that the scattered wave propagates towards the $+z$ or the $-z$ direction, respectively.

$$\mathbf{E}_x^{\mathrm{surf}} = -\frac{j\omega\eta_0}{2d^2}\left[p_x + \mathrm{sgn}(z)\, c_0^{-1} m_y\right] e^{-jk|z|}\,\hat{\mathbf{x}}, \qquad \mathbf{E}_y^{\mathrm{surf}} = -\frac{j\omega\eta_0}{2d^2}\left[p_y - \mathrm{sgn}(z)\, c_0^{-1} m_x\right] e^{-jk|z|}\,\hat{\mathbf{y}}. \quad (11b)$$

Evidently, for every one of the four different incident fields of Fig. 1, a set of induced dipole moments is derived, and subsequently, a set of scattered fields, whose computation at $z = \pm l$ leads to the reflection/transmition coefficients (or equivalently the S-parameters) of the 2D array. So, regarding the latter, if we use the evaluation scheme of [18–20], the induced dipole moments are given by

$$\boldsymbol{\mu}_1^{\mathrm{A}} = \frac{jd^2}{\omega\eta_0}\left\{\begin{bmatrix}-1\\0\\0\\-1\end{bmatrix} + \begin{bmatrix}1&1&0&0\\0&0&1&1\\0&0&1&-1\\-1&1&0&0\end{bmatrix}\begin{bmatrix}R_-^{\mathrm{A,co}}\\T_+^{\mathrm{A,co}}\\R_-^{\mathrm{A,cr}}\\T_+^{\mathrm{A,cr}}\end{bmatrix} e^{j2k_0 l}\right\}, \quad (12a)$$

$$\boldsymbol{\mu}_2^{\mathrm{A}} = \frac{jd^2}{\omega\eta_0}\left\{\begin{bmatrix}-1\\0\\0\\1\end{bmatrix} + \begin{bmatrix}1&1&0&0\\0&0&1&1\\0&0&1&-1\\-1&1&0&0\end{bmatrix}\begin{bmatrix}T_-^{\mathrm{A,co}}\\R_+^{\mathrm{A,co}}\\T_-^{\mathrm{A,cr}}\\R_+^{\mathrm{A,cr}}\end{bmatrix} e^{j2k_0 l}\right\}, \quad (12b)$$

$$\boldsymbol{\mu}_1^{\mathrm{B}} = \frac{jd^2}{\omega\eta_0}\left\{\begin{bmatrix}0\\-1\\1\\0\end{bmatrix} + \begin{bmatrix}1&1&0&0\\0&0&1&1\\0&0&1&-1\\-1&1&0&0\end{bmatrix}\begin{bmatrix}R_-^{\mathrm{B,cr}}\\T_+^{\mathrm{B,cr}}\\R_-^{\mathrm{B,co}}\\T_+^{\mathrm{B,co}}\end{bmatrix} e^{j2k_0 l}\right\}, \quad (12c)$$

$$\boldsymbol{\mu}_2^{\mathrm{B}} = \frac{jd^2}{\omega\eta_0}\left\{\begin{bmatrix}0\\-1\\-1\\0\end{bmatrix} + \begin{bmatrix}1&1&0&0\\0&0&1&1\\0&0&1&-1\\-1&1&0&0\end{bmatrix}\begin{bmatrix}T_-^{\mathrm{B,cr}}\\R_+^{\mathrm{B,cr}}\\T_-^{\mathrm{B,co}}\\R_+^{\mathrm{B,co}}\end{bmatrix} e^{j2k_0 l}\right\}, \quad (12d)$$

where superscripts "co" and "cr" stand for the parallel and normal polarization, respectively, between the scattered and the incident field, while subscripts "+" and "−" denote that the reflection/transmission coefficients are meassured at the right and left side of the 2D array, respectively, as in Fig. 2. The preceding equations can be combined into the following matrix form of

$$[M_{\mathrm{t}}] = \frac{jd^2}{\omega\eta_0}\big([F_2] + [F_3][S]e^{j2k_0 l}\big), \tag{13a}$$

where

$$[F_2] = \begin{bmatrix} -1 & -1 & 0 & 0 \\ 0 & 0 & -1 & -1 \\ 0 & 0 & 1 & -1 \\ -1 & 1 & 0 & 0 \end{bmatrix}, \quad [F_3] = \begin{bmatrix} 1 & 1 & 0 & 0 \\ 0 & 0 & 1 & 1 \\ 0 & 0 & 1 & -1 \\ -1 & 1 & 0 & 0 \end{bmatrix}, \quad [S] = \begin{bmatrix} R_-^{\mathrm{A,co}} & T_-^{\mathrm{A,co}} & R_-^{\mathrm{B,cr}} & T_-^{\mathrm{B,cr}} \\ T_+^{\mathrm{A,co}} & R_+^{\mathrm{A,co}} & T_+^{\mathrm{B,cr}} & R_+^{\mathrm{B,cr}} \\ R_-^{\mathrm{A,cr}} & T_-^{\mathrm{A,cr}} & R_-^{\mathrm{B,co}} & T_-^{\mathrm{B,co}} \\ T_+^{\mathrm{A,cr}} & R_+^{\mathrm{A,cr}} & T_+^{\mathrm{B,co}} & R_+^{\mathrm{B,co}} \end{bmatrix}, \tag{13b}$$

which compactly provides all possible excited dipoles in terms of the reflection/transmission coefficients, when the 2D array is illuminated by the plane waves of Fig. 1.

2.3. Polarizability Retrieval of a Small Scatterer

Based on the previous analysis, the desired polarizabilities can, now, be extracted in a way analogous to the techniques of [18–20]. Therefore, if (13) are inserted into (8), one arrives at

$$[\alpha]^{-1} = -\frac{j\omega\eta_0}{d^2}\,[F_1]\left([F_2] + [F_3][S]e^{j2k_0 l}\right)^{-1} + C_0\, I. \tag{14}$$

The necessary reflection/transmission coefficients in Eq. (14) can be acquired from either numerical simulations or measurements. Specifically, the measurement setups may be sufficiently large 2D particle arrays, normally illuminated by means of horn antennas at a suitable distance or smaller arrays placed into large parallel plate waveguides. Moreover, the metallic particles can be printed onto transparent membranes [27] or carefully positioned with thin transparent strings [21] in order to closely approximate the free-standing particle array scenario of the theoretical analysis. It is mentioned that in this paper, all inputs are obtained through numerical simulations. Essentially, the featured methodology can extract all the 16 polarizabilities of the scatterer, under study, at the xy-plane. For the remaining 20 unknown polarizabilities at the xz- and yz-plane, it suffices to accordingly rotate the scatterer with regard to the initial coordinate system and conduct the necessary index replacements in the related equations. In particular: (a) for the xz-plane, 90° rotation around y-axis and substitution of index x with z as well as z with x and (b) for the yz-plane, 90° rotation around x-axis and substitution of index y with z as well as z with $-y$. Hence, all the 36 elements of the full $[\alpha]$ matrix can be successfully extracted.

Furthermore, it is noteworthy to stress that due to its generalized formulation, our technique can be applied to any small scatterer, which may be modeled as a sum of dipole moments set to its center, as in Fig. 1, for the maximum number of 36 polarizabilities. However, there are a few instances where all 36 unknowns are required to be exctracted, since most scatterers used in metamaterial and artificial media applications possess fewer polarizabilities. The most common family of such particles are the simple bianisotropic or omega-type ones, which exhibit bianisotropy on a single plane or, in other words, there is a magnetoelectric coupling only between a single electric and a single magnetic dipole moment, perpendicular to each other, on a plane defined by these dipoles. Prominent members of the omega-type bianisotropic particle family are the split ring resonators (SRRs) and the omega particles [28]. These scatterers have non zero values only for the $\alpha_{ee}^{xx}, \alpha_{em}^{xy}, \alpha_{me}^{yx}, \alpha_{mm}^{yy}$, and α_{ee}^{zz} polarizabilities, with respect to the axes of Fig. 1, implying that they can be represented solely by the p_x, m_y, and p_z dipole moments. As a consequence, when placed at the 2D array setup of Fig. 1, the 4 unknown polarizabilities of the scatterer can be efficiently retrieved only via the illumination of the $\mathbf{f}_{\mathrm{A},1}^{\mathrm{inc}}$ and $\mathbf{f}_{\mathrm{A},2}^{\mathrm{inc}}$ of (9b) or through the $R_-^{\mathrm{A,co}}, T_-^{\mathrm{A,co}}, T_+^{\mathrm{A,co}}$, and $R_+^{\mathrm{A,co}}$ coefficients, in a fashion similar to other retrieval works on anisotropic or omega-type scatterers [18, 19]. In this framework, by applying the aforesaid simplifications to Eqs. (8), (9), (13), and (14), the latter reduce to

$$\begin{bmatrix} \alpha_{ee}^{xx} & \alpha_{em}^{xy} \\ \alpha_{me}^{yx} & \alpha_{mm}^{yy} \end{bmatrix}^{-1} = \begin{bmatrix} 1 & 1 \\ 1 & -1 \end{bmatrix} \begin{bmatrix} p_{x,1}^{\mathrm{A}} & p_{x,2}^{\mathrm{A}} \\ c_0^{-1} m_{y,1}^{\mathrm{A}} & c_0^{-1} m_{y,2}^{\mathrm{A}} \end{bmatrix}^{-1} + \begin{bmatrix} C_0 & 0 \\ 0 & C_0 \end{bmatrix}, \tag{15a}$$

$$\begin{bmatrix} p_{x,1}^{\mathrm{A}} & p_{x,2}^{\mathrm{A}} \\ c_0^{-1} m_{y,1}^{\mathrm{A}} & c_0^{-1} m_{y,2}^{\mathrm{A}} \end{bmatrix} = \begin{bmatrix} -1 & -1 \\ -1 & 1 \end{bmatrix} + \begin{bmatrix} 1 & 1 \\ -1 & 1 \end{bmatrix} \begin{bmatrix} R_{-}^{\mathrm{A,co}} & T_{-}^{\mathrm{A,co}} \\ T_{+}^{\mathrm{A,co}} & R_{+}^{\mathrm{A,co}} \end{bmatrix} e^{j2k_0 l}. \tag{15b}$$

Obviously, the results from Eq. (15) are the same as those extracted through the algorithm of [19], yet without the cumbersome solution of a non-linear system of equations by means of a Newton-Raphson scheme. This dimensionality reduction process of the initial formulas can be, reliably, employed for a number of polarizabilites larger than four, as in the case of wire helices [28]. Furthermore, the proposed method may effectively treat configurations with scatterers modeled via dipoles, placed away from the shape-center, by appropriately shifting the dipoles in Eq. (12), as described in [20] for a helix particle [28].

3. RESULTS AND VALIDATION

In order to verify the featured methodology, the full polarizability matrix of several complex metamaterial particles is extracted. The specific scatterers are selected to have an involved geometry, so that their polarizabilities cannot be analytically obtained [11, 40] or accurately approximated at higher frequencies by means of circuit models [12, 29]. To this aim, the required reflection/transmission coefficients input from the illuminated 2D array of the scatterer, under investigation, are acquired through numerical simulations, for every plane until the full polarizability matrix is retrieved. All metallic parts of the particles are considered to be perfect electric conductors (PEC), a convention which significantly accelerates the simulation process and constitutes an excellent approximation of metals at microwave frequencies, where the proposed algorithm is applied. However, Eqs. (14) and (15) are equivalently applicable to lossy metallic or dielectric scatterers. Moreover, in all configurations, the particle is placed on the square periodic array of Fig. 1 with $d = 10\,\mathrm{mm}$ in terms of the proper periodic boundary conditions. The reference plane for the reflection/transmission coefficients is set at $l = 0$. Then, the radar cross section (RCS) and the total radiated power (TRP) are calculated via the results of our technique for several incident plane waves impinging on an isolated scatterer (see Appendix B). The RCS and TRP, so derived, are, next, compared with their numerically computed counterparts to certify the performance of the featured formulation as well as to identify the frequency limits of the dipole approximation for different incidence angles; a procedure usually omitted in relevant works [16, 23]. Finally, it is mentioned that all numerical simulations are performed through the CST MWS$^{\mathrm{TM}}$ computational package [30]. In particular, for the extraction of the polarizability matrix, the finite element solver of the package is utilized, where the dimensions of the tetrahedra are set $\lambda/30$ near the model and at $\lambda/4$ in the rest of the computational domain. Moreover, adaptive mesh refinement is employed, while the error threshold is set to 0.01 for the S-parameters and the relative one to 0.02% for the electromagnetic field quantities. On the other hand, all simulated RCS were acquired via the method of moments solver of the package, where the surface element dimension is set to $\lambda/30$ and the accuracy iterative solver pause criterion is set to 0.001.

3.1. Omega-Type Bianisotropic Example

The first planar scatterer is the square three-turns spiral resonator (3-SR) of Fig. 3. Spirals are well known in microwave engineering as a means to reduce the electrical size of components [31]. Furthermore, they are not invariable to inversion, being asymmetrical to a plane, and thus, they exhibit omega-type bianisotropic effects similar to those of SRRs and Omega resonators. Note that the electromagnetic response of the square 3-SR has been studied in [32] via an approximate circuit model, which basically did not account for any bianisotropic effects. Such a quasi-static analysis has provided acceptable results for the determination of the first resonance frequency, yet not for the scatterer's polarizabilities [33].

Having placed the 3-SR on the 2D array setup of Fig. 1 and illuminated it by the $\mathbf{f}_{\mathrm{A},1}^{\mathrm{inc}}$ and $\mathbf{f}_{\mathrm{A},2}^{\mathrm{inc}}$ plane waves, the numerically derived reflection/transmission coefficients are depicted in Fig. 4. Due to the reciprocity of passive resonators, it holds that $T_{-}^{\mathrm{A,co}} = T_{+}^{\mathrm{A,co}}$, but owing to bianisotropy $R_{-}^{\mathrm{A,co}} \neq R_{+}^{\mathrm{A,co}}$, as shown in Fig. 4(b), where $\arg(R_{-}^{\mathrm{A,co}}) \neq \arg(R_{+}^{\mathrm{A,co}})$. Subsequently, the reflection/transmission coefficients are inserted into Eq. (15) and the 3-SR polarizabilies are presented in Fig. 5. Note that the results are

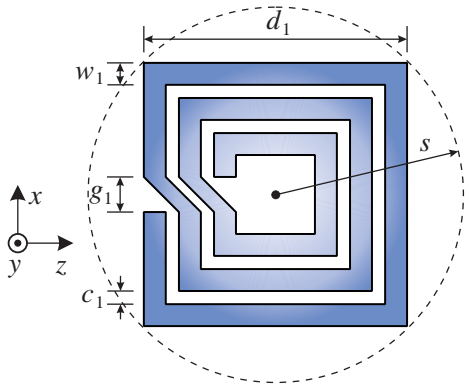

Figure 3. Geometry and coordinate system definition of the square 3-SR, with $d_1 = 6\,\text{mm}$, $g_1 = 0.8\,\text{mm}$, and $w_1 = c_1 = 0.5\,\text{mm}$. The thickness of the metallic strips is $t = 0.02\,\text{mm}$, while $s = \sqrt{2}d_1/2$ is the minimum radius of a virtual sphere that encloses the particle and $2s$ the largest particle dimension.

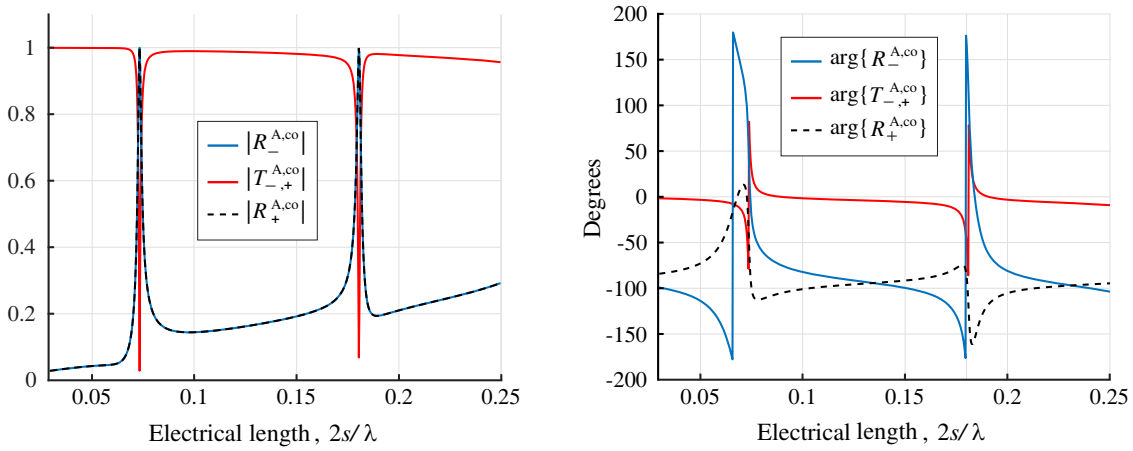

Figure 4. Reflection/transmission coefficients from the 2D array of Fig. 1, consisting of square 3-SRs with the dimensions provided in Fig. 3. (a) Magnitude and (b) phase.

in accordance with the Onsager-Casimir symmetries [28,34], as $\alpha_{em}^{xy} = -\alpha_{me}^{yx}$. Furthermore, if the 3-SR is twisted 90° around the y-axis and repeat the extraction procedure, the unknown α_{ee}^{zz} is obtained, which does not exhibit any resonace, while at low frequencies it holds that $\alpha_{ee}^{zz} \approx \alpha_{ee}^{xx}$; an outcome that is in full accordance with previous reports on SRRs [28,33].

The efficiency of our technique for the square 3-SR setup is, next, examined by means of various RCS and TRP comparisons. In addition, to pursue the relation of the extracted polarizabilities with wavevector $\mathbf{k}$, five ψ_A or ψ_B incidence angles are considered for the respective TM,1 and TE,2 modes, namely the 90° (TEM incidence), 60°, 45°, 30° and 0°, according to Fig. B1 (see Appendix B). Owing to the planar geometry of the 3-SR, these are the only modes which can excite all the elements of $[\alpha]$ and induce the required p_x, m_y, and p_z dipoles. Notice that other mode selections induce either no dipoles or solely the p_z one and therefore lead to a trivial analysis. In this context, Figs. 6–10 illustrate the polar diagrams of the calculated and simulated RCS for $\theta = \pi/2$[†]. Specifically, in Figs. 6 and 7, the RCS are depicted for large wavelengths in comparison to the dimensions of the scatterers and in the vicinity of the first resonance, i.e., at $2s/\lambda \approx 0.055$ (or $f = 1.936\,\text{GHz}$) and $2s/\lambda \approx 0.071$ (or $f = 2.515\,\text{GHz}$), respectively. As observed, the calculated results are in excellent agreement with those obtained via numerical simulations, certifying that the dipole approximation of a

[†] Although $\theta = \pi/2$ is the maximum radiation plane for the p_x dipole, the selection of θ is purely arbitrary and indicative. Hence, this validation procedure can be successfully conducted for any θ or φ.

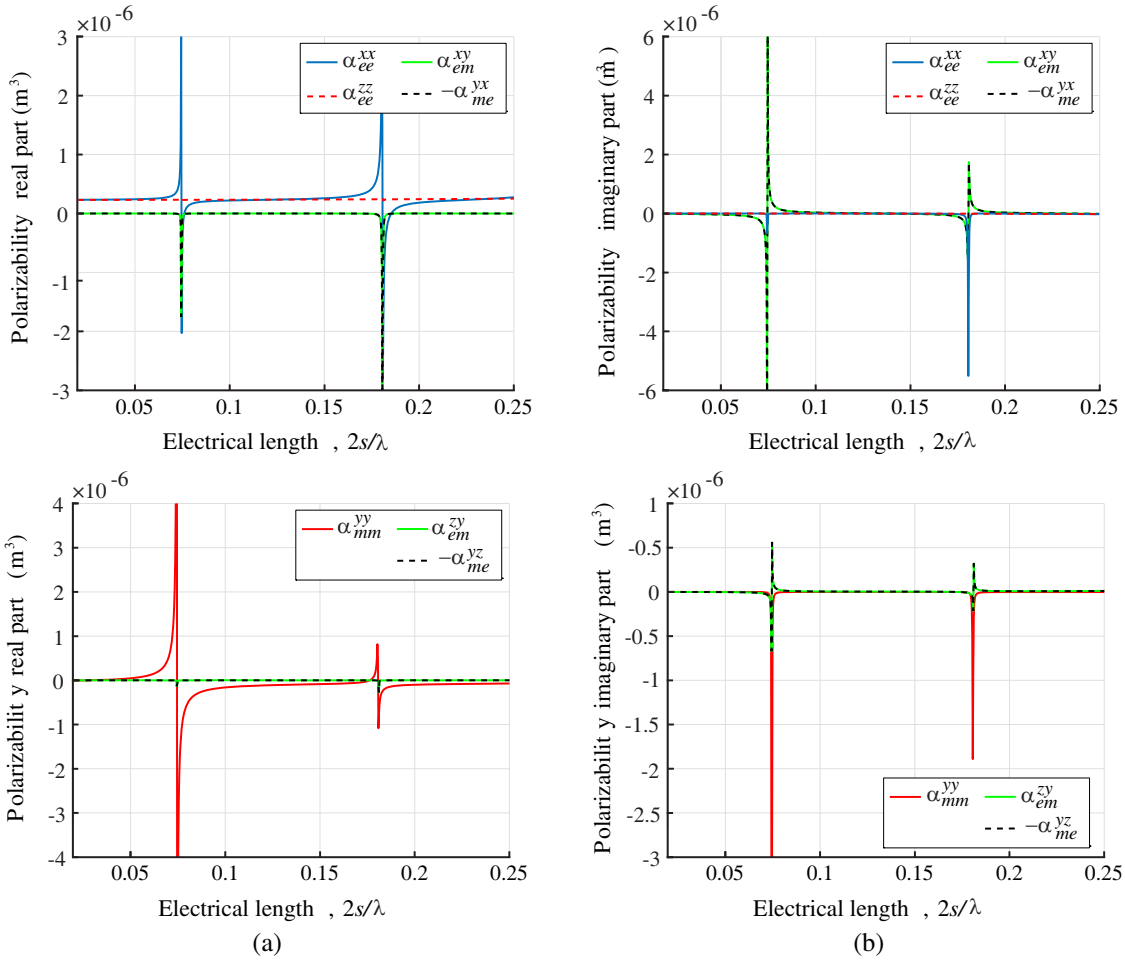

Figure 5. Polarizabilities of the square 3-SR computed through the proposed method. (a) Real and (b) imaginary parts.

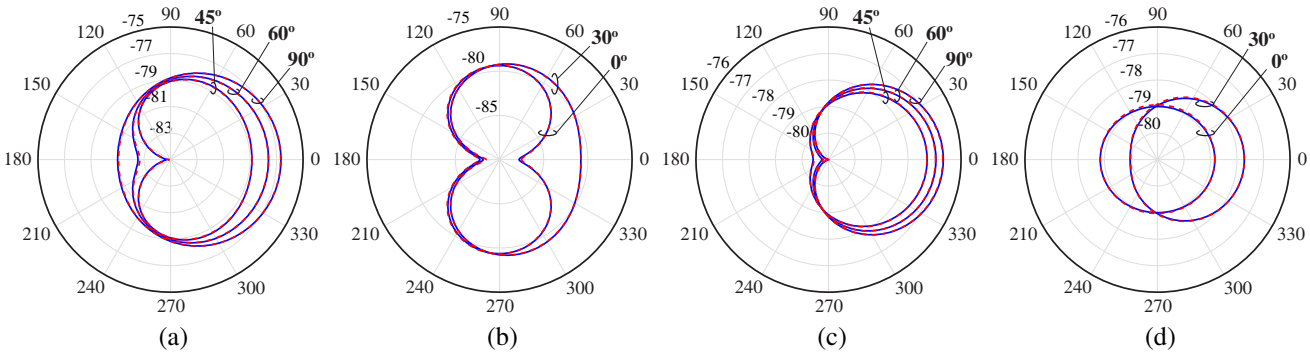

Figure 6. Calculated (blue solid line) through the proposed method and numerically retrieved (red dashed line) RCS polar patterns (in dB) versus φ ($\theta = \pi/2$) (in deg) of the square 3-SR at $f = 1.936$ GHz (or $2s/\lambda \approx 0.055$) for (a) a TM,1 incidence with $\psi_{\mathrm{A}} = 90°, 60°, 45°$, (b) a TM,1 incidence with $\psi_{\mathrm{A}} = 30°, 0°$, (c) a TE,2 incidence with $\psi_{\mathrm{B}} = 90°, 60°, 45°$ and (d) a TE,2 incidence with $\psi_{\mathrm{B}} = 30°, 0°$.

particle in the quasi-static region ($\sim 0.1\lambda$) is, indeed, notably accurate. Moving to smaller wavelengths, Fig. 8 shows an equivalently promising match at $2s/\lambda \approx 0.14$ (or $f = 4.951$ GHz). Also in Fig. 9, approaching the second resonance, a very good coincidence between the results is retained, especially

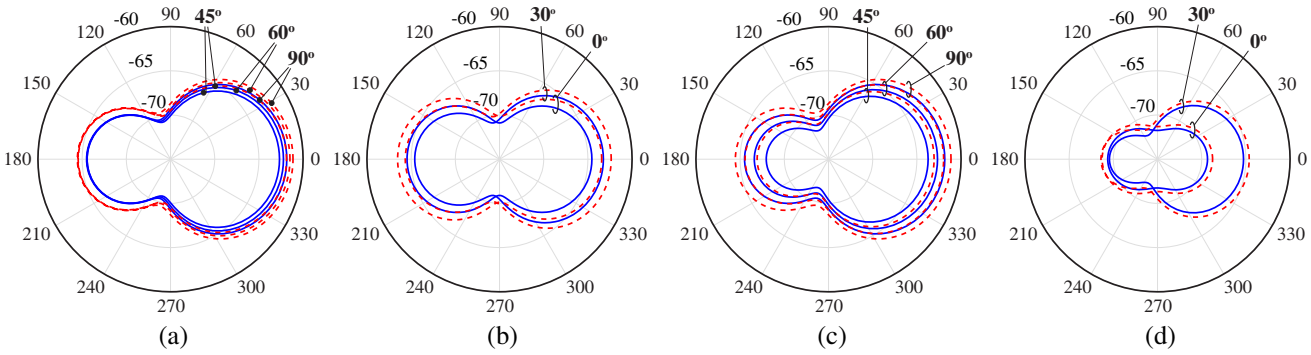

Figure 7. Calculated (blue solid line) through the proposed method and numerically retrieved (red dashed line) RCS polar patterns (in dB) versus φ ($\theta = \pi/2$) (in deg) of the square 3-SR at $f = 2.515\,\text{GHz}$ (or $2s/\lambda \approx 0.071$) for (a) a TM,1 incidence with $\psi_\text{A} = 90°, 60°, 45°$, (b) a TM,1 incidence with $\psi_\text{A} = 30°, 0°$, (c) a TE,2 incidence with $\psi_\text{B} = 90°, 60°, 45°$, and (d) a TE,2 incidence with $\psi_\text{B} = 30°, 0°$.

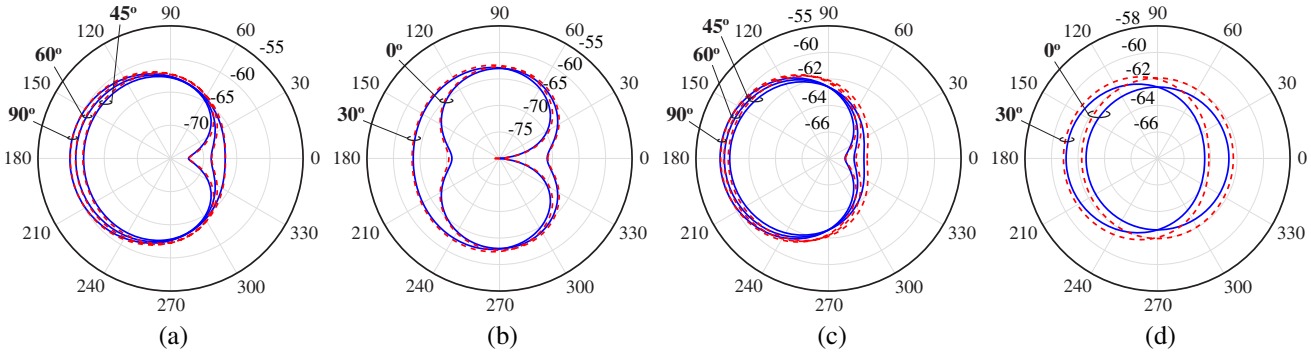

Figure 8. Calculated (blue solid line) through the proposed method and numerically retrieved (red dashed line) RCS polar patterns (in dB) versus φ ($\theta = \pi/2$) (in deg) of the square 3-SR at $f = 4.951\,\text{GHz}$ (or $2s/\lambda \approx 0.14$) for (a) a TM,1 incidence with $\psi_\text{A} = 90°, 60°, 45°$, (b) a TM,1 incidence with $\psi_\text{A} = 30°, 0°$, (c) a TE,2 incidence with $\psi_\text{B} = 90°, 60°, 45°$, and (d) a TE,2 incidence with $\psi_\text{B} = 30°, 0°$.

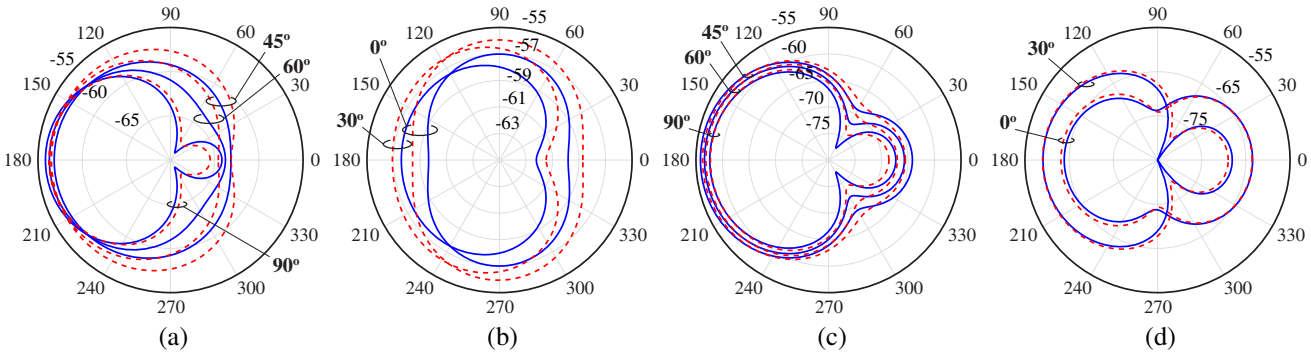

Figure 9. Calculated (blue solid line) through the proposed method and numerically retrieved (red dashed line) RCS polar patterns (in dB) versus φ ($\theta = \pi/2$) (in deg) of the square 3-SR at $f = 6.575\,\text{GHz}$ (or $2s/\lambda \approx 0.186$) for (a) a TM,1 incidence with $\psi_\text{A} = 90°, 60°, 45°$, (b) a TM,1 incidence with $\psi_\text{A} = 30°, 0°$, (c) a TE,2 incidence with $\psi_\text{B} = 90°, 60°, 45°$, and (d) a TE,2 incidence with $\psi_\text{B} = 30°, 0°$.

at $2s/\lambda \approx 0.186$ (or $f = 6.575\,\text{GHz}$). Finally, the RCS comparisons are provided, at $2s/\lambda \approx 0.24$ (or $f = 8.475\,\text{GHz}$), in Fig. 10, i.e., near the empirical limit for the dipole approximation ($\sim \lambda/4$), and right after the second resonance. Again, the computed RCS outcomes and the simulated ones exhibit

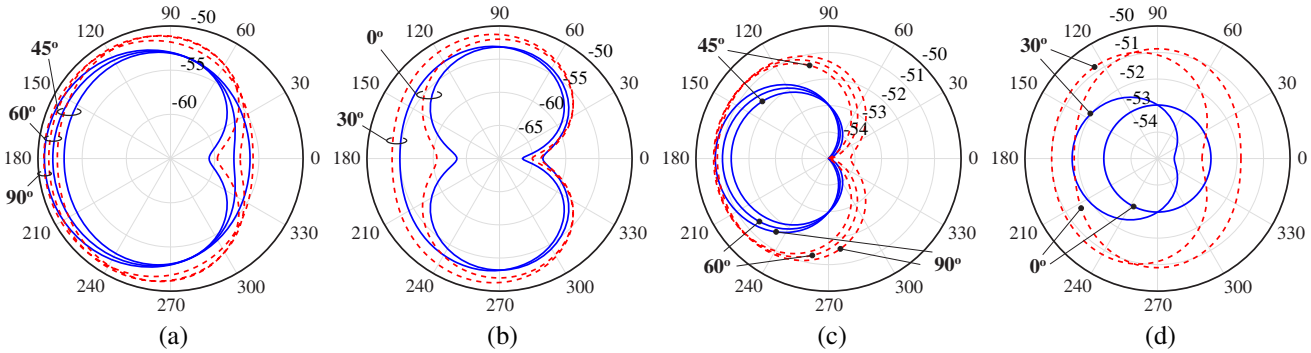

Figure 10. Calculated (blue solid line) through the proposed method and numerically retrieved (red dashed line) RCS polar patterns (in dB) versus φ ($\theta = \pi/2$) (in deg) of the square 3-SR at $f = 8.475$ GHz (or $2s/\lambda \approx 0.24$) for (a) a TM,1 incidence with $\psi_{\mathrm{A}} = 90°, 60°, 45°$, (b) a TM,1 incidence with $\psi_{\mathrm{A}} = 30°, 0°$, (c) a TE,2 incidence with $\psi_{\mathrm{B}} = 90°, 60°, 45°$, and (d) a TE,2 incidence with $\psi_{\mathrm{B}} = 30°, 0°$.

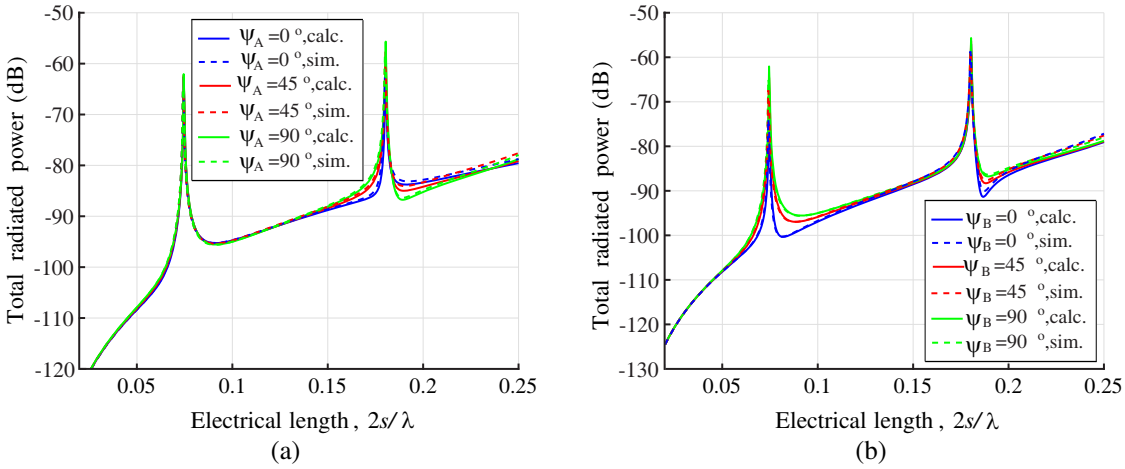

Figure 11. Calculated (solid lines) through the proposed method and numerically retrieved (dashed lines) TRP patterns of the square 3-SR for (a) a TM,1 incidence with $\psi_{\mathrm{A}} = 90°, 45°, 0°$ and (b) a TE,2 incidence with $\psi_{\mathrm{B}} = 90°, 45°, 0°$.

a satisfactory match for the TM,1 modes, unlike the TE,2 case, where the dipole approximation is proven inadequate. Actually, in previous studies of the surface current distribution for SRR structures, that can be deemed geometrically similar to the SR ones, it has been reported that a quadrupole term is induced near the second resonance [28, 33]. Hence, in order to expand the proposed methodology beyond the $\lambda/4$ limit, a quadrupole is added in our formulation, particularly for the 3-SR regarding the TE,2 incidence and as a function of the k_y component. Fig. 11 displays the comparison between the calculated and simulated TRP responses of the square 3-SR, and as detected its total scattered power is excellently modeled for both the first and second resonances. In this way, the featured algorithm offers a trustworthy description of the particle's scattering behavior for electrical dimensions in the area of $\lambda/5$.

3.2. A Generalized Example

The simplified version of the proposed technique, as presented in Eq. (15), is typically sufficient for the majority of the scatterers used in artificial media applications. Nonetheless, when more demanding scatterers are examined, with either a full polarizability matrix or much more elements than those of the previous 3-SR example, the generalized extraction technique of Eqs. (13) and (14) should be

employed. These equations are, also, selected when the scatterer involves an unknown number of significant (non-zero) polarizabilities prior to the retrieval procedure. Since in its full form, $[\alpha]$ has 36 unknown elements, the specific method must be successively applied to the xy-, yz-, and xz-plane, so that all the necessary polarizabilities are determined. Among potential candidates for our study, helices constitute the simplest particles for constructing a chiral material. In fact, they are composed of 3D thin metallic wire spirals, with right- or left-hand turns, which determine the polarization angle rotation [28,35]. Fig. 12 depicts a variation of a two-turns right-handed spiral, i.e., the non-planar chiral resonator [36]. Specifically, herein, the spirals of the resonator are connected using a via; a very useful feature for PCB realizations [37].

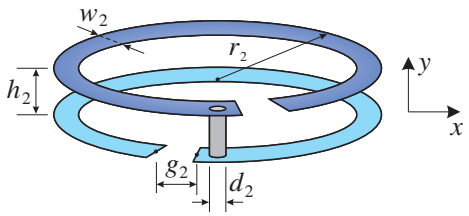

Figure 12. Geometry and coordinate system definition of the via chiral quasi-planar particle, with $r_2 = 3.5\,\text{mm}$, $h_2 = 1\,\text{mm}$, $g_2 = 0.5\,\text{mm}$, $d_2 = 0.3\,\text{mm}$, and $w_2 = c_2 = 0.5\,\text{mm}$. The thickness of the metallic strips is $t = 0.02\,\text{mm}$, while $s = \sqrt{(h_2/2)^2 + r_2^2}$ is the minimum radius of a virtual sphere that encloses the particle and $2s$ the largest particle dimension.

Let us, firstly, proceed with the extraction of the polarizabilities of the quasi-planar resonator in Fig. 12. Taking into account previous modeling attempts of such resonators and the geometry of the problem, $[\alpha]$ has as non-zero elements, at least all the polarizabilities at the xy-plane along with α_{ee}^{zz} and α_{mm}^{zz} [33, 36]. So, the generalized algorithm of subsection 2.3 for the xy-plane and any of the xz- or yz-plane is deemed sufficient. However, in this paper, the aforesaid technique is applied to every plane in order to extract all the 36 elements of $[\alpha]$. In this framework, the reflection/transmission coefficients regarding the structure of Fig. 12, placed onto the 2D array of Fig. 1, for the xy-plane and the E_x or "A" incident polarization, are shown in Fig. 13. The bianisotropy of the particle is evident, as $R_-^{\text{A,co}} \neq R_+^{\text{A,co}}$, while its chiral nature is confirmed from the existence of cross-polarization field components. Furthermore, the polarizabilities of the particle for the xy-plane are calculated by inserting the reflection/transmission coefficients into Eq. (14). Then, the scatterer is rotated by 90° around the y- as well as the x-axis, and the retrieval algorithm is applied consecutively until all polarizabilities are acquired, as shown in Fig. 14. Explicitly, only the main polarizabilities of the resonator, also provided in the relevant literature, are given, since the others are significantly smaller (around 10^{-8}-10^{-9}) and, thus, they can be safely neglected. Moreover, the Onsager-Casimir symmetries are successfully verified, i.e., $\alpha_{ee}^{ij} = \alpha_{ee}^{ji}$, $\alpha_{mm}^{ij} = \alpha_{mm}^{ji}$, $\alpha_{em}^{ii} = -\alpha_{me}^{ii}$ and $\alpha_{em}^{ij} = -\alpha_{me}^{ji}$, for $i, j = x, y$ with $i \neq j$. Observe that at low frequencies, it holds that $\alpha_{ee}^{xx} \approx \alpha_{ee}^{zz}$, which has, also, been reported in existing works [33, 36].

Since matrix $[\alpha]$ is full and in order to be excited as a whole, the RCS for all the incident modes of Fig. B1 (see Appendix B) should be calculated, i.e., TM,1, TE,1, TM,2, and TE,2. Then, the polar diagrams of the computed and simulated RCS for $\theta = \pi/2$ and incidence angles 90°, 60°, 45°, 30°, and 0° are illustrated in Figs. 15–18. Concentrating on the results from the TM modes in Figs. 15(a) and Fig. 16(a), an excellent agreement is attained for low frequencies, as well, specifically at $f = 2.5\,\text{GHz}$ (or $2s/\lambda \approx 0.0507$). Our outcomes are, also, satisfactory in Figs. 15(b) and 16(b), that is at $f = 3.5\,\text{GHz}$ (or $2s/\lambda \approx 0.071$), athough some numerical discrepancies can be discerned, mainly due to abrupt polarizability variations near the resonance. On the other hand, the convergence between the computed and simulated RCS in Figs. 15(c) and 16(c) remains very promising beyond the first resonance at $f = 5\,\text{GHz}$ (or $2s/\lambda \approx 0.101$), while only after $\lambda/6$, namely at $f = 8\,\text{GHz}$ (or $2s/\lambda \approx 0.162$) in Figs. 15(d) and 16(d), the dipole approximation begins to slightly deteriorate, as shown in Fig. 16(d), yet still prooving its high efficiency as a powerful modeling tool, even in rather demanding cases. Moving to the TE mode results, a notable match is observed in Figs. 17(a) and 18(a) at $f = 2.5\,\text{GHz}$ (or $2s/\lambda \approx 0.0507$), whereas a very sufficient convergence at $f = 3.5\,\text{GHz}$ (or $2s/\lambda \approx 0.071$) occurs in Figs. 17(b) and 18(b).

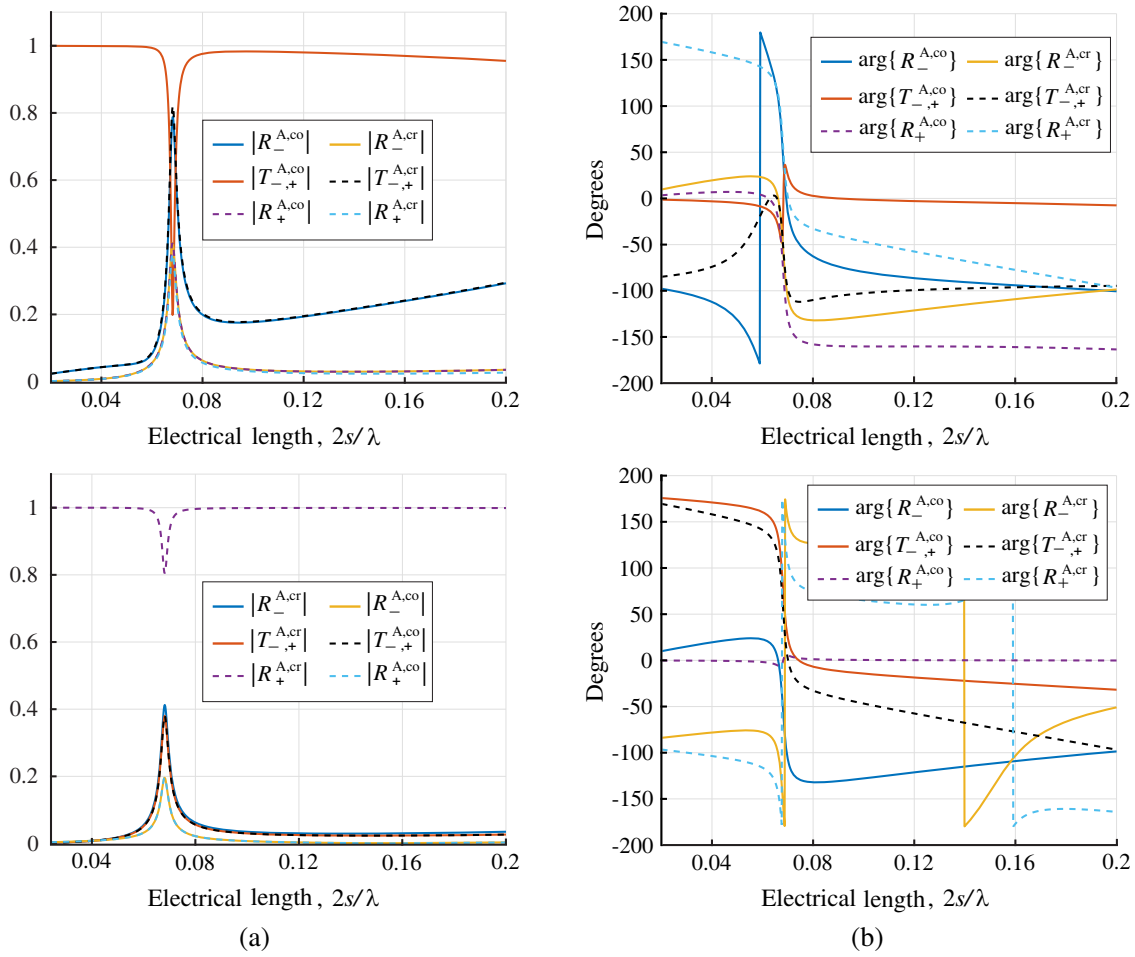

Figure 13. Reflection/transmission coefficients from the 2D array of Fig. 1, consisting of via chiral quasi-planar particles with dimensions provided in Fig. 12. (a) Magnitude and (b) phase.

Moreover, at $f = 5\,\text{GHz}$ (or $2s/\lambda \approx 0.101$), the RCS outcomes retain their excellent agreement for the TE,1 incidences (Fig. 17(c)), unlike the TE,2 mode ones, where some deviations appear (Fig. 18(c)). In addition, the dipole approximation begins to collapse beyond $\lambda/6$, at $f = 8\,\text{GHz}$ (or $2s/\lambda \approx 0.162$), as indicated in Figs. 17(d) and 18(d). Lastly, Fig. 19 presents the calculated and simulated TRP results for the via chiral quasi-planar particle and all incident modes. It is promptly observed that the proposed methodology accomplishes a very good prediction of the scatterer's behavior before and around the first resonance, i.e., the most important frequency region for modern applications, with some small numerical deviations concerning the resonance location, as, also, detected in the respective RCS outcomes. The latter deviations increase gradually for electrical sizes beyond $\lambda/6$, until the final collapse of the dipole approximation at $\lambda/5$. This is principally attributed to the geometry of the scatterer, since for sufficiently high incident wave frequencies, the individual feature dimensions of the particle cannot be considered "small". Consequently, not all the induced currents correspond to electric or magnetic dipoles, an issue which cancels the validity of the dipole approximation.

4. CONCLUSIONS AND FUTURE ASPECTS

A generalized algorithm for extracting the full polarizability matrix of an arbitrary small scatterer via the reflection/transmission coefficients has been introduced. First, it was presumed that the particle, under study, is sufficiently small in relation to the wavelength of the impinging wave, so that it can be modeled through electric and magnetic dipoles. Subsequently, the arbitrary scatterer

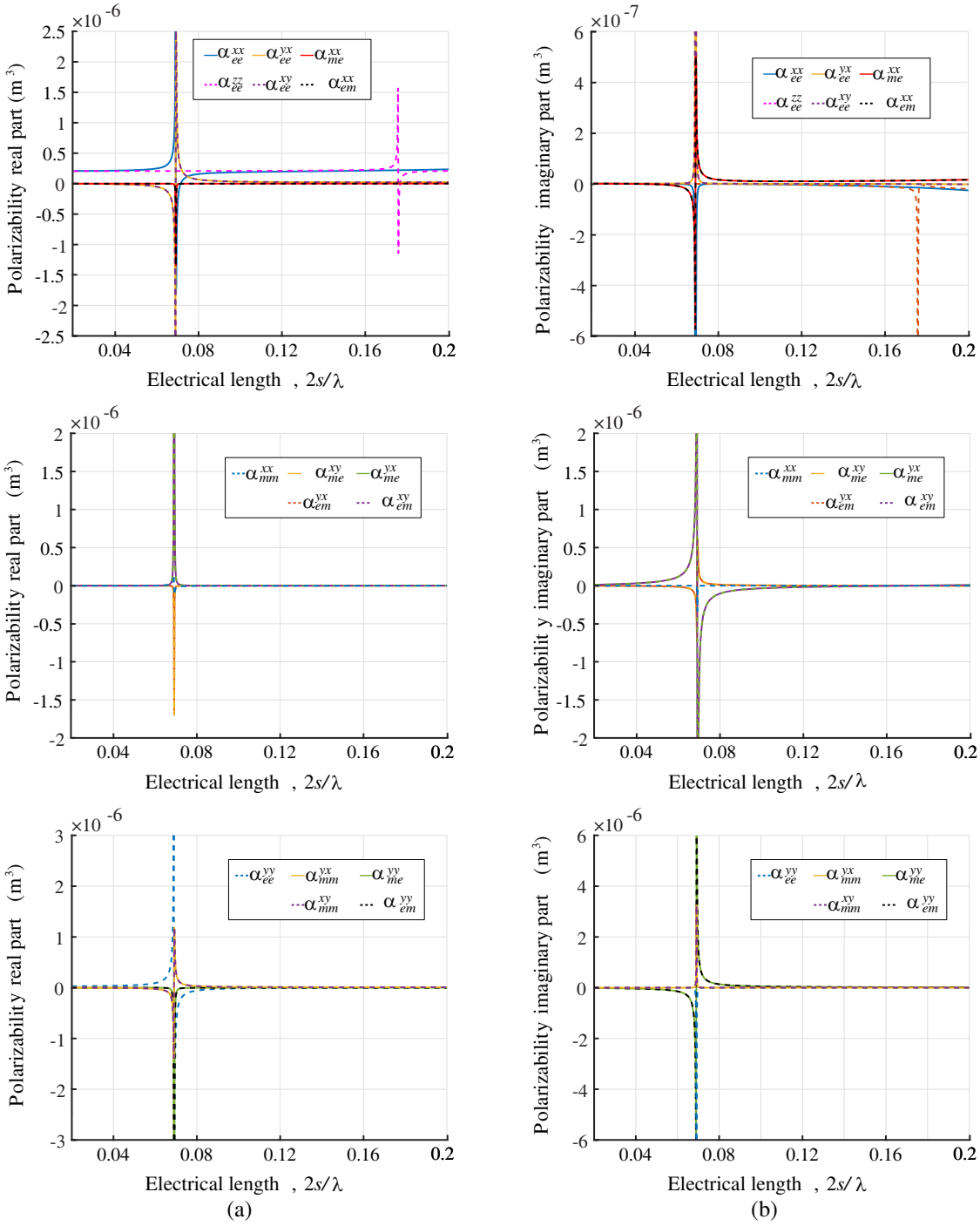

Figure 14. Reflection/transmission coefficients from the 2D array of Fig. 1, consisting of via chiral quasi-planar particles with dimensions provided in Fig. 12. (a) Magnitude and (b) phase.

is placed on a 2D square lattice, illuminated, on both sides, with normally incident plane waves of two polarizations perpendicular to each other. Considering the field interactions on the array, the excited dipoles are expressed as a function of the reflection/transmission coefficients from the array, and the full polarizability matrix is efficiently calculated. Furthermore, a simplified version of the prior technique for omega-type bianisotropic scatterers has been developed, as a straightforward means for the majority of particles involved in contemporary metamaterial configurations. For its verification,

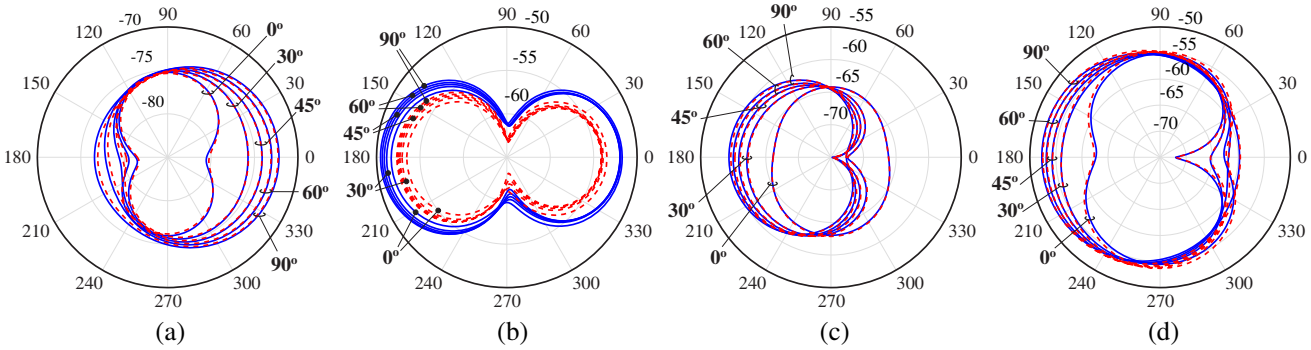

Figure 15. Calculated (blue solid line) through the proposed method and numerically retrieved (red dashed line) RCS polar patterns (in dB) versus φ ($\theta = \pi/2$) (in deg) of the via chiral quasi-planar particle for a TM,1 incidence with $\psi_{\mathrm{A}} = 90°, 60°, 45°, 30°, 0°$ at (a) $f = 2.5\,\mathrm{GHz}$ (ot $2s/\lambda \approx 0.05$), (b) $f = 3.5\,\mathrm{GHz}$ (or $2s/\lambda \approx 0.071$), (c) $f = 5\,\mathrm{GHz}$ (or $2s/\lambda \approx 0.101$), and (d) $f = 8\,\mathrm{GHz}$ (or $2s/\lambda \approx 0.162$).

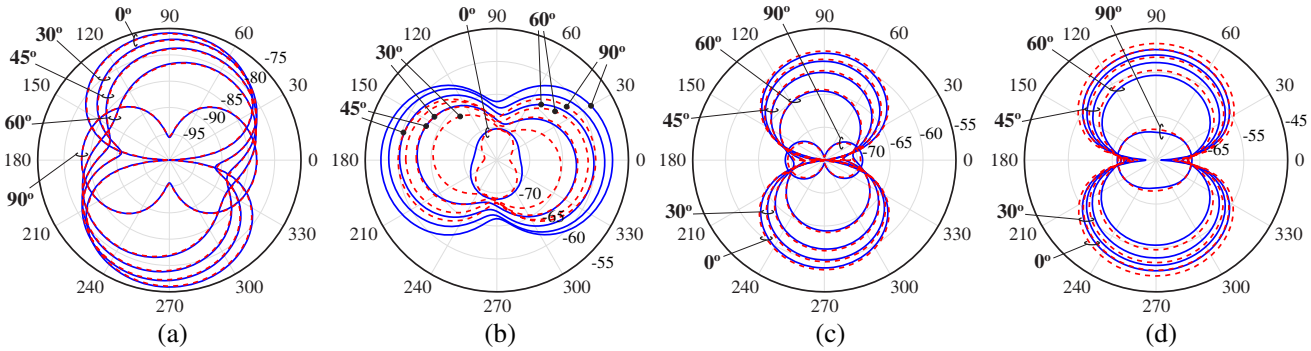

Figure 16. Calculated (blue solid line) through the proposed method and numerically retrieved (red dashed line) RCS polar patterns (in dB) versus φ ($\theta = \pi/2$) (in deg) of the via chiral quasi-planar particle for a TM,2 incidence with $\psi_{\mathrm{A}} = 90°, 60°, 45°, 30°, 0°$ at (a) $f = 2.5\,\mathrm{GHz}$ (or $2s/\lambda \approx 0.05$), (b) $f = 3.5\,\mathrm{GHz}$ (or $2s/\lambda \approx 0.071$), (c) $f = 5\,\mathrm{GHz}$ (or $2s/\lambda \approx 0.101$), and (d) $f = 8\,\mathrm{GHz}$ (or $2s/\lambda \approx 0.162$).

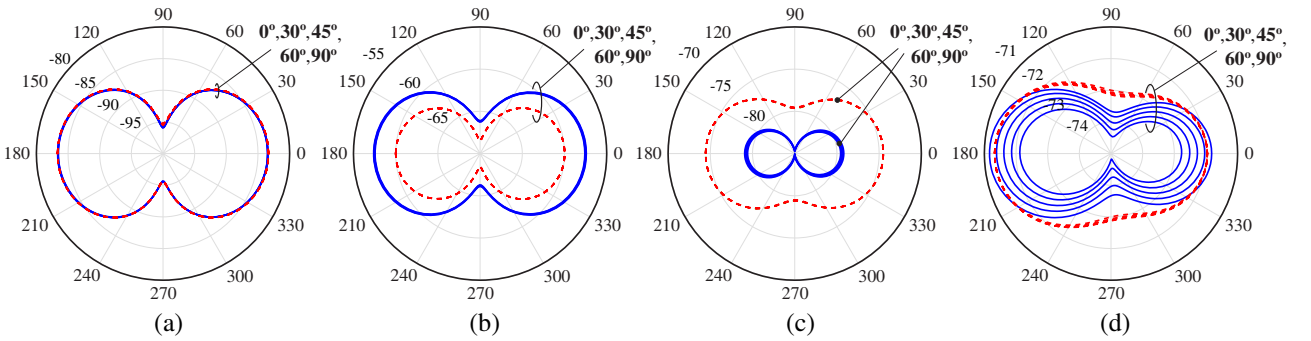

Figure 17. Calculated (blue solid line) through the proposed method and numerically retrieved (red dashed line) RCS polar patterns (in dB) versus φ ($\theta = \pi/2$) (in deg) of the via chiral quasi-planar particle for a TE,1 incidence wuth $\psi_{\mathrm{A}} = 90°, 60°, 45°, 30°, 0°$ at (a) $f = 2.5\,\mathrm{GHz}$ (or $2s/\lambda \approx 0.05$), (b) $f = 3.5\,\mathrm{GHz}$ (or $2s/\lambda \approx 0.071$), (c) $f = 5\,\mathrm{GHz}$ (or $2s/\lambda \approx 0.101$), and (d) $f = 8\,\mathrm{GHz}$ (or $2s/\lambda \approx 0.162$).

the proposed methodology has been comprehensively applied to demanding metamaterial scatterers in order to evalaute the RCS and TRP of the structures, which were then compared with simulated counterparts. The polarizabilities, so retrieved, are deemed "natural", in the sense that they obey to

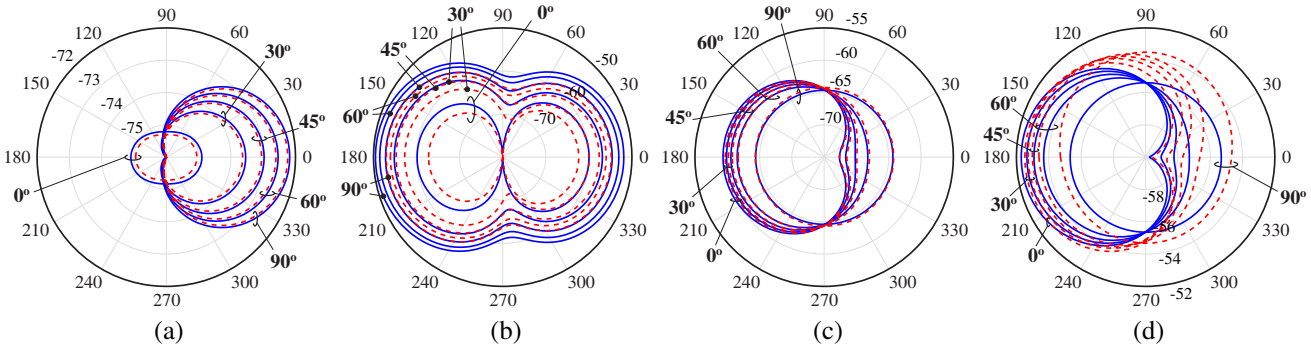

Figure 18. Calculated (blue solid line) through the proposed method and numerically retrieved (red dashed line) RCS polar patterns (dB) versus φ ($\theta = \pi/2$) (in deg) of the via chiral quasi-planar particle for a TE,2 incidence with $\psi_{\rm A} = 90°, 60°, 45°, 30°, 0°$ at (a) $f = 2.5\,{\rm GHz}$ (or $2s/\lambda \approx 0.05$), (b) $f = 3.5\,{\rm GHz}$ (or $2s/\lambda \approx 0.071$), (c) $f = 5\,{\rm GHz}$ (or $2s/\lambda \approx 0.101$), and (d) $f = 8\,{\rm GHz}$ (or $2s/\lambda \approx 0.162$).

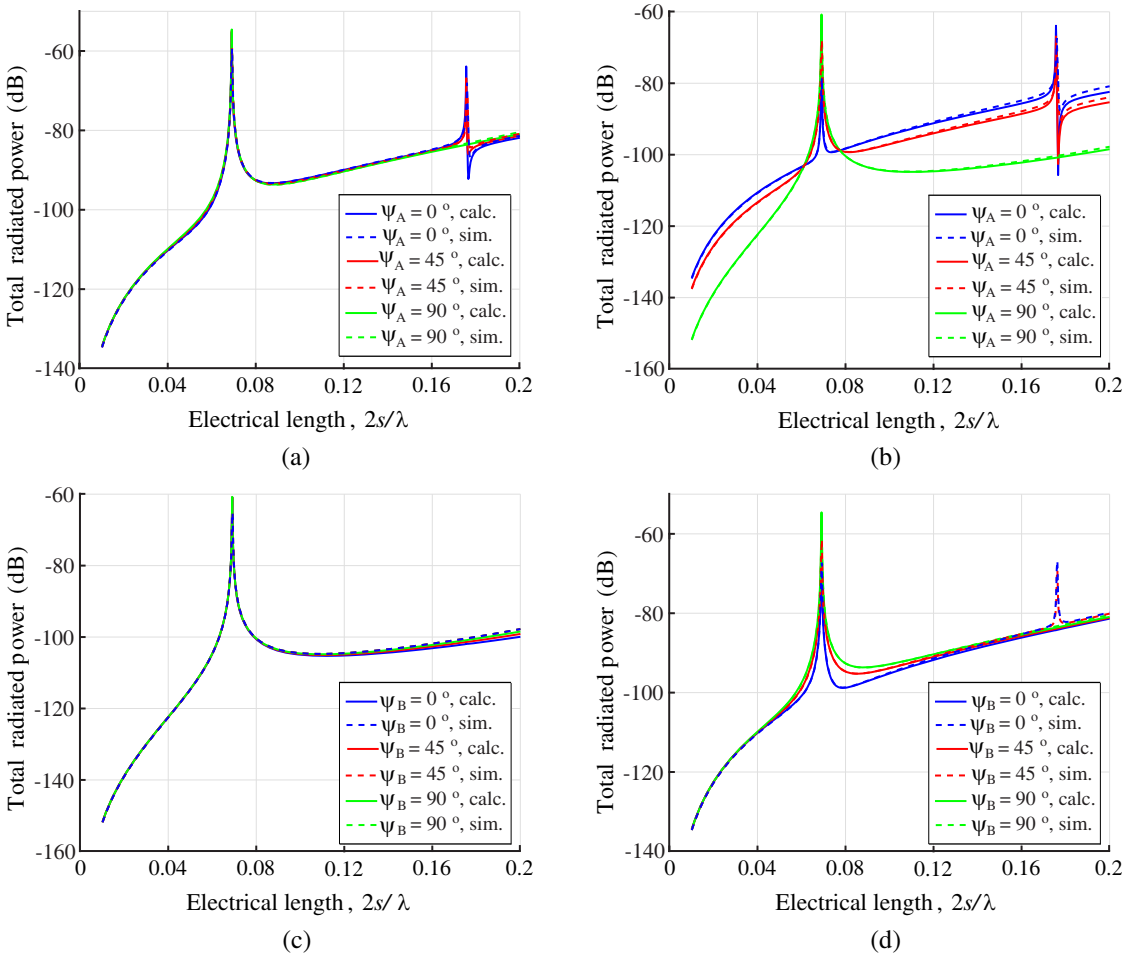

Figure 19. Calculated (solid lines) through the proposed method and numerically retrieved (dashed lines) TRP patterns of the via chiral quasi-planar particle for (a) a TM,1 incidence with $\psi_{\rm A} = 90°, 45°, 0°$, (b) a TM,2 incidence with $\psi_{\rm A} = 90°, 45°, 0°$, (c) a TE,1 incidence with $\psi_{\rm B} = 90°, 45°, 0°$, and (d) a TE,2 incidence with $\psi_{\rm B} = 90°, 45°, 0°$.

all theoretical symmetries and are in complete accordance with the findings of existing analytical or circuit-modeling efforts. Moreover, the RCS and TRP comparisons certified the notable competences of the dipole approximation, at least up to $\lambda/5$, which is usually the homogenization limit.

Regarding future endeavors, the conclusions from this work can lead to further research in various directions. Essentially, the featured paper is meant to present the complete theoretical framework for the polarizability matrix extraction via reflection/transmission coefficients, and thus all the required data originated from numerical simulations. Nonetheless, a future work involving polarizability extraction through measurements and the implications the latter may exhibit, such as the fabrication of the required scatterer arrays and the selection of the proper instrumentation, would be quite instructive. As already implied, the main drawback of the dipole approximation is the convention that all other terms, except the dipole ones, are negligible. However, as one approaches $\lambda/6$, these terms become progressively significant, until the collapse of the dipole approximation near $\lambda/4$, where, as shown in our examples, an electric quadrupole is actually excited. So, to expand in frequency the multipole representation of a scatterer's response, the quadrupole contribution must be considered. The first way to conduct this task is to incorporate the quadrupole terms in the extraction model and retrieve the respective quadrupolarizability elements [11]. Such a process may be quite complex and requires the reformulation of the resulting equations to account for the quadrupole interactions [38, 39], yet, initially, simpler dielectric sphere examples with analytically known quadruple terms, may be studied [40–42]. Alternatively, to maintain the present concept to some extent, "equivalent" polarizabilities can be defined. To this goal, by twisting the particle on the 2D array and applying the featured algorithm, an "equivalent" polarizability matrix, or $[\alpha(f, \mathbf{k})]$, can be constructed. In the light of this relaxation for the polarizability definition, the accuracy of the dipole approximation could be significantly enhanced, without having to modify the initial analysis tool presented, herein.

APPENDIX A. CO-FIELD INTERACTION COEFFICIENTS

In Fig. 1, an orthonormal lattice of scatterers is constructed on the xy-plane at $z = 0$. If the comprising scatterers are electrically small, they can be replaced with the respective induced dipoles from an impinging wave, $\mathbf{p}(x, y) = \mathbf{p}(as, bl)$ and $\mathbf{m}(x, y) = \mathbf{m}(as, bl)$, where $\{s, l\} = 0, \pm1, \pm2, ...$ integers indicating the coordinates of the dipoles along the x- and y-axis, respectively. Let us assume an impinging wave on the 2D array with a wavevector $\mathbf{q} = q_x\hat{\mathbf{x}} + q_y\hat{\mathbf{y}} + q_z\hat{\mathbf{z}}$. Then, owing to the orthogonal symmetry, the Bloch theorem can be applied for the dipole moments [7, 43] in the form of

$$\mathbf{p}(as, bl) = \mathbf{p}_0 e^{-j\mathbf{qr}} u(\mathbf{r}) = \mathbf{p}_0 e^{-j(q_x as + q_y bl)}\, \delta(x - as)\delta(y - bl), \tag{A1a}$$

$$\mathbf{m}(as, bl) = \mathbf{m}_0 e^{-j\mathbf{qr}} u(\mathbf{r}) = \mathbf{m}_0 e^{-j(q_x as + q_y bl)}\, \delta(x - as)\delta(y - bl), \tag{A1b}$$

with $\mathbf{p}_0$ and $\mathbf{m}_0$ the induced dipoles at the origin of the axes. For simplicity and without loss of generality, the interaction of the array scatterers is calculated, herein, at $O(0, 0, 0)$[‡]. Utilizing dyadic Green's functions [24, 43], the scattered fields from all particles on the array are computed as

$$\mathbf{E}^{\text{scat}} = \iint_{S'} jk_0\eta_0 \bar{\bar{G}}_{\text{co}}(\mathbf{r}, \mathbf{r}') \cdot \mathbf{J}(\mathbf{r}')\mathrm{d}S' + \iint_{S'} \bar{\bar{G}}_{\text{cr}}(\mathbf{r}, \mathbf{r}') \cdot \mathbf{K}(\mathbf{r}')\mathrm{d}S', \tag{A2a}$$

$$\mathbf{H}^{\text{scat}} = -\iint_{S'} \bar{\bar{G}}_{\text{cr}}(\mathbf{r}, \mathbf{r}') \cdot \mathbf{J}(\mathbf{r}')\mathrm{d}S' + \iint_{S'} \frac{jk_0}{\eta_0} \bar{\bar{G}}_{\text{co}}(\mathbf{r}, \mathbf{r}') \cdot \mathbf{K}(\mathbf{r}')\mathrm{d}S', \tag{A2b}$$

with the free space dyadic Green's functions given by

$$\bar{\bar{G}}_{\text{co}}(\mathbf{r}, \mathbf{r}') = -\left(\bar{\bar{I}} + \frac{\nabla\nabla}{k_0^2}\right), \quad \bar{\bar{G}}_{\text{cr}}(\mathbf{r}, \mathbf{r}') = \nabla \times \bar{\bar{G}}_{\text{co}}(\mathbf{r}, \mathbf{r}') = -\left(\nabla \times \bar{\bar{I}}\right), \quad g(\mathbf{r}, \mathbf{r}') = \frac{e^{-jk_0|\mathbf{r}-\mathbf{r}'|}}{4\pi|\mathbf{r} - \mathbf{r}'|}. \tag{A3}$$

[‡] Results from the analysis at the origin of the axes are the same as for any other point on the lattice with the appropriate phase addition $e^{-j(q_x as + q_y bl)}$.

The electric and magnetic current surface densities $\mathbf{J}(\mathbf{r}')$ and $\mathbf{K}(\mathbf{r}')$ are, then, calculated via Eq. (A1), by excluding the dipoles at $O(0,0,0)$[§], namely

$$\mathbf{J}(\mathbf{r}') = j\omega\mathbf{P}(\mathbf{r}') = \frac{j\omega}{\delta S}\sum_{(s,l)\neq(0,0)}\sum \mathbf{p}_0 e^{-j(q_x as+q_y bl)}u(x,y), \tag{A4a}$$

$$\mathbf{K}(\mathbf{r}') = j\omega\mu_0\mathbf{M}(\mathbf{r}') = \frac{j\omega\mu_0}{\delta S}\sum_{(s,l)\neq(0,0)}\sum \mathbf{m}_0 e^{-j(q_x as+q_y bl)}u(x,y), \tag{A4b}$$

where δS is the surface unit for the density calculation, set equal to $1\,\mathrm{m}^2$. Substituting Eqs. (A3) and (A4a) into Eq. (A2), as well as the distance from $O(0,0)$ on the 2D array, $\mathbf{r}-\mathbf{r}' = as\hat{\mathbf{x}}+bl\hat{\mathbf{y}}$, one arrives at

$$\varepsilon_0\mathbf{E}^{\mathrm{scat}}_{(0,0)} = \bar{\bar{C}}\cdot\mathbf{p}_0 + \bar{\bar{C}}_{em}\cdot c_0^{-1}\mathbf{m}_0, \qquad c_0^{-1}\mathbf{H}^{\mathrm{scat}}_{(0,0)} = -\bar{\bar{C}}_{em}\cdot\mathbf{p}_0 + \bar{\bar{C}}\cdot c_0^{-1}\mathbf{m}_0, \tag{A5}$$

with $\bar{\bar{C}}$ and $\bar{\bar{C}}_{em}$ the co-field and cross-field interaction coefficient tensors, respectively, calculated via

$$\bar{\bar{C}} = \sum_{(s,l)\neq(0,0)}\sum\Big(k_0^2\bar{\bar{I}}+\nabla\nabla\Big)g(\mathbf{r},\mathbf{r}')e^{-j(q_x as+q_y bl)}, \qquad \bar{\bar{C}}_{em} = \sum_{(s,l)\neq(0,0)}\sum -jk_0\left(\nabla\times\bar{\bar{I}}\right)g(\mathbf{r},\mathbf{r}')e^{-j(q_x as+q_y bl)}, \tag{A6}$$

for $\bar{\bar{I}} = \hat{\mathbf{x}}\hat{\mathbf{x}}+\hat{\mathbf{y}}\hat{\mathbf{y}}+\hat{\mathbf{z}}\hat{\mathbf{z}}$ the unitary dyad. Finally, through identity $(\nabla\times\bar{\bar{I}})^T = -\nabla\times\bar{\bar{I}}$, it follows from (A6) that $\bar{\bar{C}}^T = \bar{\bar{C}}$ and $\bar{\bar{C}}^T_{em} = -\bar{\bar{C}}_{em}$. Obviously, $\bar{\bar{C}} = \bar{\bar{C}}_{ee} = \bar{\bar{C}}_{mm}$ and $\bar{\bar{C}}_{em} = \bar{\bar{C}}_{em} = -\bar{\bar{C}}_{me}$, if the notation of Eq. (4) is employed. So, the dyadic components can be obtained in terms of Eq. (A6) and it is derived that $C^{xz} = C^{zx} = C^{yz} = C^{zy} = 0$ as well as $C^{xx}_{em} = C^{yy}_{em} = C^{zz}_{em} = C^{xy}_{em} = C^{yx}_{em} = 0$ [26]. Additionally, owing to reciprocity and symmetry,

$$C^{yy}(k_0,q_x,q_y,a,b) = C^{xx}(k_0,q_y,q_x,b,a), \qquad C^{xz}_{em}(k_0,q_x,q_y,a,b) = -C^{yz}_{em}(k_0,q_y,q_x,b,a). \tag{A7}$$

From these expressions, it is deduced that through the initial computation of the 18 coefficients in Eq. (A6), the problem reduces to only 4 coefficients; C^{xx}, C^{xy}, C^{zz}, and C^{yz}_{em}. For the analysis of the this work, only C^{xx} and C^{xy} are presented, whereas C^{zz} and C^{yz}_{em} are omitted [7, 26]. In this context, the co-field interaction coefficient C^{xx} for a normal plane wave incidence ($q_x = q_y = 0$) on a 2D square array (Fig. 1), after the separate calculation of the interaction between the dipole moments for $y = 0$ on the x-axis [44] and the parallel series of dipole momens, is described by the converging series

$$\begin{aligned} C^{xx}(k_0,d) = &-\frac{1}{\pi d}\sum_{l=1}^{\infty}\sum_{\mathrm{Re}\{p_s\}\neq 0} p_s^2\,K_0(p_s bl) \\ &-\sum_{\mathrm{Re}\{p_s\}=0}\frac{p_s}{2d^2}\left[\frac{1}{jk^z_{s,0}}+\frac{jd}{2}-1.202\,\frac{p_s^2d^3}{8\pi^3}+\frac{d}{\pi}\left(\ln\frac{d|p_s|}{4\pi}+0.577\right)+\sum_{l=1}^{\infty}\left(\frac{1}{jk^z_{s,l}}+\frac{1}{jk^z_{s,-l}}-\frac{d}{\pi l}+\frac{p_s^2d^3}{8\pi^3l^3}\right)\right] \\ &+\frac{1}{4\pi d^3}\left[4\sum_{s=1}^{\infty}\frac{(2jk_0d+3)s+2}{s^3(s+1)(s+2)}e^{-jk_0ds}-4jk_0d\,(t_1\ln t_2)-2(jk_0d+1)\left(t_1^2\ln t_2+2e^{jk_0d}\right)+7jk_0d+3\right], \end{aligned} \tag{A8}$$

formulated in terms of several transformations [25]. In (A8),

$$\begin{aligned} k^x_s &= 2\pi s/d, \quad k^y_{\pm l} = \pm 2\pi l/d, & k^z_{s,\pm l} &= -j\sqrt{(k^x_s)^2+(k^y_{\pm l})^2-k_0^2}, \\ p_s &= \sqrt{(k^x_s)^2-k_0^2}, \quad q_s = -p_s^2, & t_1 &= 1-e^{-jk_0d}, \quad t_2 = 1-e^{jk_0d}, \end{aligned} \tag{A9}$$

and $K_0(x)$ is the modified Bessel function of the second kind, zeroth class.

Then, coefficient C^{xy} is evaluated, for the same setup (Fig. 1) from the second expression in Eq. (A6) by splitting to summations in terms of n and the use of symmetries [45], as

$$C^{xy}(k_0,d) = -\frac{j}{2d^2}\sum_{s,l}\frac{k^x_s k^y_l}{k^z_{s,l}}\frac{e^{-jk^z_{s,l}d}-1}{\cos(k^z_{s,l}d)-1}. \tag{A10}$$

Note that for a normally incident plane wave onto a square array, coefficient C^{xy} is negligible in comparison with C^{xx} or C^{yy}, as demonstrated in Fig. A1.

[§] $u(x,y) = u(\mathbf{r}) = \delta(x-as)\delta(y-bl)$.

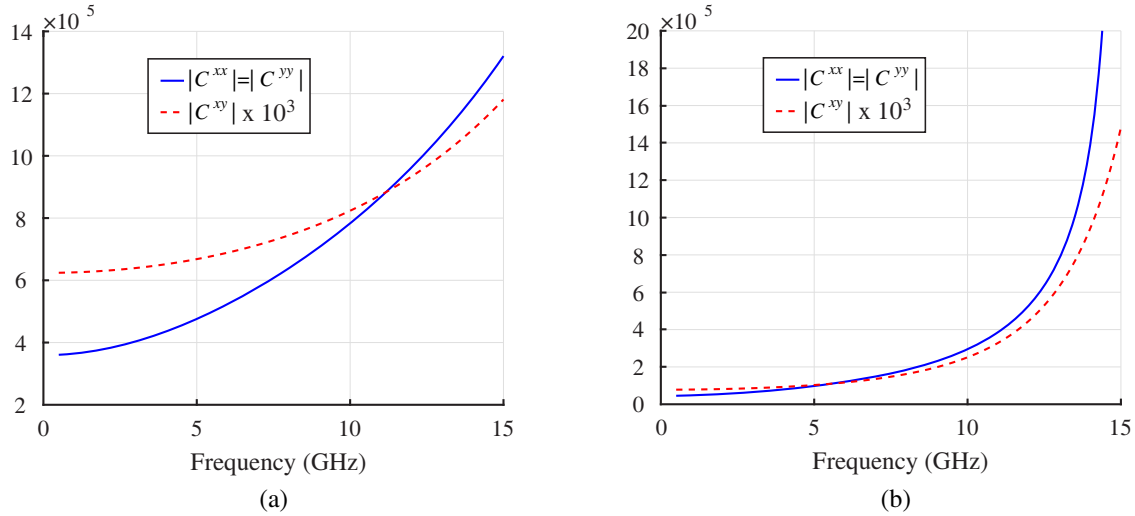

Figure A1. Co-field interaction coefficients for the setup of Fig. 1 and a square lattice of (a) $d = 10\,\text{mm}$ and (b) $d = 20\,\text{mm}$.

APPENDIX B. VALIDATION VIA THE RCS AND TRP

Given its polarizabilities, a small scatterer can be modeled as a collection of electric and magnetic dipoles, through which the surrounding fields can be computed. Specifically, by means of vector potentials [40], the field from the induced dipole moments results in

$$\mathbf{E}_{\text{p}} = \frac{k_0^2}{4\pi\varepsilon_0}\frac{e^{-jk_0r}}{r}\left\{(\hat{\mathbf{n}}\times\mathbf{p})\times\hat{\mathbf{n}} + [3\hat{\mathbf{n}}(\hat{\mathbf{n}}\cdot\mathbf{p}) - \mathbf{p}]\left(\frac{1}{r^2} - \frac{jk_0}{r}\right)\right\}, \tag{B1a}$$

$$\mathbf{E}_{\text{m}} = -\frac{k_0^2}{4\pi\varepsilon_0}\frac{e^{-jk_0r}}{r}\left(\hat{\mathbf{n}}\times c_0^{-1}\mathbf{m}\right)\left(1 - \frac{1}{jk_0r}\right), \tag{B1b}$$

where $\mathbf{E}_{\text{p}}$ and $\mathbf{E}_{\text{m}}$ are the fields due to the electric and magnetic dipole moments, respectively, while $\hat{\mathbf{n}}$ is the unit vector in the direction of the observation point. Via the far-field assumption, it holds that $(1/r^3, 1/r^2) \to 0$, thus, in the far-field region the electric field from a small scatterer, i.e., Eq. (B1) becomes

$$\mathbf{E}_{\text{rad}} = \frac{k_0^2}{4\pi\varepsilon_0}\frac{e^{-jk_0r}}{r}\left[(\hat{\mathbf{n}}\times\mathbf{p})\times\hat{\mathbf{n}} - \left(\hat{\mathbf{n}}\times c_0^{-1}\mathbf{m}\right)\right]. \tag{B2}$$

Following Eq. (B2), the respective bistatic RCS can be evaluated. The latter is defined as [43]

$$\sigma = \lim_{r\to\infty}\left(4\pi r^2\frac{|\mathbf{E}_{\text{rad}}|^2}{|\mathbf{E}_{\text{inc}}|^2}\right) \Rightarrow \sigma \lim_{r\to\infty} = \left(4\pi r^2|\mathbf{E}_{\text{rad}}|^2\right), \tag{B3}$$

where a normalized vector is utilized for the incident field or $|\mathbf{E}_{\text{inc}}| = 1$. Substitution of Eq. (B2) into Eq. (B3) yields the RCS formula, as a function of the induced dipole moments,

$$\sigma = \frac{k_0^4}{4\pi\varepsilon_0^2}|(\hat{\mathbf{n}}\times\mathbf{p})\times\hat{\mathbf{n}} - (\hat{\mathbf{n}}\times c_0^{-1}\mathbf{m})|^2. \tag{B4}$$

Finally, the TRP of a small scatterer as a function of its respective dipole moments is given by the integration of the averaged power, radiated per unit solid angle, on a full spherical surface [40], namely

$$P_t = \frac{c_0^2\,\eta_0\,k_0^4}{32\pi^2}\int_\Omega |(\hat{\mathbf{n}}\times\mathbf{p})\times\hat{\mathbf{n}} - (\hat{\mathbf{n}}\times c_0^{-1}\mathbf{m})|^2 d\Omega \tag{B5}$$

where Ω is the solid angle with a differential in spherical coordinates $d\Omega = \sin\theta d\theta d\phi$.

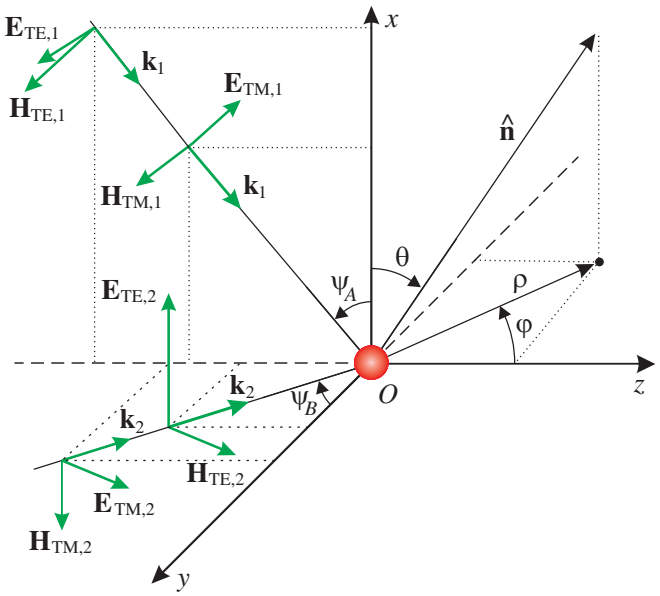

Figure B1. The RCS/TRP calculation setup. The particle, under study, is placed at the origin of the coordinate system and illuminated by two TM and two TE modes with respect to the x-, y-, and z-axis.

Let us assume that the scatterer, under study, is placed at the origin of the coordinate system, as shown in Fig. B1, with its geometric axes coinciding with the axes of the system. Moreover, the unit vector at the observation point is denoted as $\hat{\mathbf{n}} = \sin\theta\cos\varphi\,\hat{\mathbf{x}} - \sin\theta\sin\varphi\,\hat{\mathbf{y}} + \cos\theta\,\hat{\mathbf{z}}$. Then, the required dipole moments $\mathbf{p}$ and $\mathbf{m}$ are calculated via Eq. (1), and, through the orientation of Fig. B1, any arbitrary incident plane wave can be decomposed into a combination of the four depicted plane waves

$$\mathbf{f}^{\text{inc}}_{\text{TM},1} = \varepsilon_0\,[\sin\psi_{\text{A}}\;\; 0\;\; 0\;\; 1\;\; \cos\psi_{\text{A}}\;\; 0]^T\,, \qquad \mathbf{f}^{\text{inc}}_{\text{TE},1} = \varepsilon_0\,[0\;\; -\sin\psi_{\text{A}}\;\; 1\;\; 0\;\; 0\;\; -\cos\psi_{\text{A}}]^T\,, \tag{B6a}$$

$$\mathbf{f}^{\text{inc}}_{\text{TM},2} = \varepsilon_0\,[0\;\; -1\;\; \sin\psi_{\text{B}}\;\; 0\;\; \cos\psi_{\text{B}}\;\; 0]^T\,, \qquad \mathbf{f}^{\text{inc}}_{\text{TE},2} = \varepsilon_0\,[1\;\; 0\;\; 0\;\; \sin\psi_{\text{B}}\;\; 0\;\; \cos\psi_{\text{B}}]^T\,. \tag{B6b}$$

Thus, after the extraction of $[\alpha]$ via the proposed technique, the induced dipoles are obtained from Eq. (1) for various angles ψ_{A} and ψ_{B}. In this manner, the acquired $\mathbf{p}$ and $\mathbf{m}$ are utilized for the determination of the RCS through Eq. (B4), as a function of (θ, φ), or the TRP through Eq. (B5).

REFERENCES

1. Silveirinha, M. G., "Generalized Lorentz-Lorentz formulas for microstructured materials," *Phys. Rev. B*, Vol. 76, No. 24, 245117, 2007.
2. Alù, A., "First-principles homogenization theory for periodic metamaterials," *Phys. Rev. B*, Vol. 84, No. 7, 075153, 2011.
3. Liu, X. X. and A. Alù, "Generalized retrieval method for metamaterial constitutive parameters based on a physically driven homogenization approach," *Phys. Rev. B*, Vol. 87, No. 23, 235136, 2013.
4. Karamanos, T. D., S. D. Assimonis, A. I. Dimitriadis, and N. V. Kantartzis, "Effective parameter extraction of 3D metamaterial arrays via first-principles homogenization theory," *Photonics Nanostructures: Fundam. Appl.*, Vol. 12, No. 4, 291–297, 2014.
5. Simovski, C. R., B. Sauviac, and S. L. Prosvirnin, "Homogenization of an array of S-shaped particles located on a dielectric interface," *Progress In Electromagnetics Research*, Vol. 39, 249–264, 2003.
6. Mohamed, M. A., E. F. Kuester, M. Piket-May, and C. L. Holloway, "The field of an electric dipole and the polarizability of a conducting object embedded in the interface between dielectric materials," *Progress In Electromagnetics Research B*, Vol. 16, 1–20, 2009.

7. Dimitriadis, A. I., N. V. Kantartzis, T. D. Tsiboukis, and C. Hafner, "Generalized non-local surface susceptibility model and Fresnel coefficients for the characterization of periodic metafilms with bianisotropic scatterers," *J. Comput. Phys.*, Vol. 281, 251–268, 2015.
8. Andryieuski, A., A. V. Lavrinenko, M. Petrov, and S. A. Tretyakov, "Homogenization of metasurfaces formed by random resonant particles in periodical lattices," *Phys. Rev. B*, Vol. 93, No. 20, 205127, 2016.
9. Dimitriadis, A. I., T. D. Karamanos, N. V. Kantartzis, and T. D. Tsiboukis, "Effective-surface modeling of infinite periodic metascreens exhibiting the extraordinary transmission phenomenon," *J. Opt. Soc. Am. B*, Vol. 33, No. 3, 434–444, 2016.
10. Alaee, R., M. Albooyeh, and C. Rockstuhl, "Theory of metasurface based perfect absorbers," *J. Phys. D: Appl. Phys.*, Vol. 50, No. 50, 503002, 2017.
11. Sihvola, A. H., *Electromagnetic Mixing Formulas and Applications*, IET Publishers, Stevenage, 1999.
12. Marqués, R., F. Mesa, J. Martel, and F. Medina, "Comparative analysis of edge-and broadside-coupled split ring resonators for metamaterial design-theory and experiments," *IEEE Trans. Antennas Propag.*, Vol. 51, No. 10, 2572–2581, 2003.
13. Mirmoosa, M., Y. Ra'di, V. Asadchy, C. Simovski, and S. Tretyakov, "Polarizabilities of nonreciprocal bianisotropic particles," *Phys. Rev. Appl.*, Vol. 1, No. 3, 034005, 2014.
14. Terekhov, Y. E., A. V. Zhuravlev, and G. V. Belokopytov, "The polarizability matrix of split-ring resonators," *Moscow Univ. Phys. Bull.*, Vol. 66, 254–259, 2011.
15. Yazdi, M. and N. Komjani, "Polarizability tensor calculation using induced charge and current distributions," *Progress In Electromagnetics Research M*, Vol. 45, 123–130, 2016.
16. Asadchy, V. S., I. A. Faniayeu, Y. Ra'di, and S. A. Tretyakov, "Determining polarizability tensors for an arbitrary small electromagnetic scatterer," *Photonics Nanostructures: Fundam. Appl.*, Vol. 12, No. 4, 298–304, 2014.
17. Alaee, R., M. Albooyeh, M. Yazdi, N. Komjani, C. Simovski, F. Lederer, and C. Rockstuhl, "Magnetoelectric coupling in nonidentical plasmonic nanoparticles: Theory and applications," *Phys. Rev. B*, Vol. 91, 115119, 2015.
18. Scher, A. D. and E. F. Kuester, "Extracting the bulk effective parameters of a metamaterial via the scattering from a single planar array of particles," *Metamaterials*, Vol. 3, No. 1, 44–55, 2009.
19. Karamanos, T. D., A. I. Dimitriadis, and N. V. Kantartzis, "Robust technique for the polarisability matrix retrieval of bianisotropic scatterers via their reflection and transmission coefficients," *IET Microw. Antennas Propag.*, Vol. 8, No. 15, 1398–1407, 2014.
20. Karamanos, T. and N. Kantartzis, "Polarizability matrix retrieval of a non-planar chiral particle through scattering parameters," *Appl. Phys. A*, Vol. 122, No. 4, 378, 2016.
21. Jelinek, L. and J. Machac, "A polarizability measurement method for electrically small particles," *IEEE Antennas Wireless Propag. Lett.*, Vol. 13, 1051–1053, 2014.
22. Pulido-Mancera, L., P. T. Bowen, M. F. Imani, N. Kundtz, and D. Smith, "Polarizability extraction of complementary metamaterial elements in waveguides for aperture modeling," *Phys. Rev. B*, Vol. 96, No. 23, 235402, 2017.
23. Liu, X.-X., Y. Zhao, and A. Alù, "Polarizability tensor retrieval for subwavelength particles of arbitrary shape," *IEEE Trans. Antennas Propag.*, Vol. 64, No. 6, 2301–2310, 2016.
24. Tai, C.-T., *Dyadic Green Functions in Electromagnetic Theory*, IEEE Press, Piscataway, 1994.
25. Belov, P. A. and C. R. Simovski, "Homogenization of electromagnetic crystals formed by uniaxial resonant scatterers," *Phys. Rev. E*, Vol. 72, No. 2, 026615, 2005.
26. Scher, A. and E. Kuester, "Boundary effects in the electromagnetic response of a metamaterial in the case of normal incidence," *Progress In Electromagnetics Research B*, No. 14, 341–381, 2009.
27. Lee, S., B. Kang, H. Keum, N. Ahmed, J. Rogers, P. Ferreira, S. Kim, and B. Min, "Heterogeneously assembled metamaterials and metadevices via 3D modular transfer printing," *Sci. Rep.*, Vol. 6, 27621, 2016.

28. Serdyukov, A., I. Semchenko, S. Tretyakov, and A. Sihvola, *Electromagnetics of Bi-anisotropic Materials: Theory and Applications*, Gordon and Breach, Amsterdam, 2001.
29. Withayachumnankul, W., C. Fumeaux, and D. Abbott, "Compact electric-LC resonators for metamaterials," *Opt. Express*, Vol. 18, No. 25, 25912–25921, 2010.
30. CST Microwave Studio^{TM}, *Computer Simulation Technology*, 2017.
31. Bilotti, F., A. Toscano, and L. Vegni, "Design of spiral and multiple split-ring resonators for the realization of miniaturized metamaterial samples," *IEEE Trans. Antennas Propag.*, Vol. 55, No. 8, 2258–2267, 2007.
32. Baena J. D., R. Marqués, F. Medina, and J. Martel, "Artificial magnetic metamaterial design by using spiral resonators," *Phys. Rev. B*, Vol. 69, No. 1, 014402, 2004.
33. Marqués, R., F. Martín, and M. Sorolla, *Metamaterials with Negative Parameters: Theory, Design and Microwave Applications*, John Wiley & Sons, New York, 2011.
34. Sersic, I., C. Tuambilangana, T. Kampfrath, and A. F. Koenderink, "Magnetoelectric point scattering theory for metamaterial scatterers," *Phys. Rev. B*, Vol. 83, No. 24, 245102, 2011.
35. Gansel, J. K., M. Thiel, M. S. Rill, M. Decker, K. Bade, V. Saile, G. von Freymann, S. Linden, and M. Wegener, "Gold helix photonic metamaterial as broadband circular polarizer," *Science*, Vol. 325, No. 5947, 1513–1515, 2009.
36. Marqués, R., L. Jelinek, and F. Mesa, "Negative refraction from balanced quasi-planar chiral inclusions," *Microw. Opt. Technol. Lett.*, Vol. 49, No. 10, 2606–2609, 2007.
37. Wang, B., J. Zhou, T. Koschny, and C. M. Soukoulis, "Nonplanar chiral metamaterials with negative index," *Appl. Phys. Lett.*, Vol. 94, No. 15, 151112, 2009.
38. Silveirinha, M. G., "Boundary conditions for quadrupolar metamaterials," *New J. Phys.*, Vol. 16, No. 8, 083042, 2014.
39. Yaghjian, A., "Boundary conditions for electric quadrupolar continua," *Radio Sci.*, Vol. 49, No. 12, 1289–1299, 2014.
40. Jackson, J. D., *Classical Electrodynamics*, Wiley, New York, 1999.
41. Yaghjian, A. D., M. Silveirinha, A. Askarpour, and A. Alù, "Electric quadrupolarizability of a source-driven dielectric sphere," *Progress In Electromagnetics Research B*, Vol. 63, 95–106, 2015.
42. Alaee, A., C. Rockstuhl, and I. Fernandez-Corbaton, "An electromagnetic multipole expansion beyond the long-wavelength approximation," *Opt. Commun.*, Vol. 407, 17–21, 2018.
43. Volakis, J., *Integral Equation Methods for Electromagnetics*, IET Publishers, Stevenage, 2012.
44. Weber, W. and G. Ford, "Propagation of optical excitations by dipolar interactions in metal nanoparticle chains," *Phys. Rev. B*, Vol. 70, No. 12, 125429, 2004.
45. Scher, A. D., "Boundary effects in the electromagnetic response of a metamaterial using the point-dipole interaction model," Ph.D. Thesis, University of Colorado at Boulder, Boulder, 2008.